© 2021 Katherine Anne Lakomy

FABRICATION AND PERFORMANCE OF BROAD-AREA HIGH POWER NARROW LINEWIDTH SEMICONDUCTOR LASER DIODES

BY

KATHERINE ANNE LAKOMY

DISSERTATION

Submitted in partial fulfillment of the requirements
for the degree of Doctor of Philosophy in Electrical and Computer Engineering
in the Graduate College of the
University of Illinois Urbana-Champaign, 2021

Urbana, Illinois

Doctoral Committee:

Professor Kent D. Choquette, Chair
Emeritus Professor J. Gary Eden
Professor John Dallesasse
Associate Professor Minjoo Lawrence Lee

ABSTRACT

This thesis presents the theoretical and experimental examination of broad-area, high-order, distributed feedback (DFB) grating, semiconductor laser diodes for the goal of manufacturably attaining longitudinal mode reduction. Through coupled mode theory, the coupling coefficient, the reflectivity, and the laser emission linewidth resulting from a refractive index grating are predicted. A comparison is made between lasers with coated and uncoated facets, demonstrating that the impact of DFB gratings is enhanced by facet coating. Both surface-etched and epitaxially buried DFB grating lasers emitting at 15xx nm using designs with varying grating order and fill factor, are fabricated at the Holonyak Micro and Nanotechnology Laboratory cleanroom using standard i-line optical lithography. Alternative lithography techniques are proposed without reliance on small feature definition by electron-beam lithography. The buried grating lasers are characterized in terms of threshold current, emission wavelength, and spectral linewidth. Under pulsed operation, the threshold currents of lasers diodes 30 μm wide and 2 mm cavity length are found to moderately increase using the DFB gratings. The spectral linewidths measured for buried grating lasers are less than control lasers (lacking gratings), demonstrating a reduction of longitudinal modes with high-order gratings, compatible with optical lithography. The most successful grating designs have 50% fill factor and the measured emission linewidths are consistent with theoretical estimates. This work has demonstrated 1.5 μm laser diodes with spectral narrowing arising from longitudinal mode reduction via DFB gratings, fabricated using designs and techniques amenable with high volume production. While the grating designs demonstrated in this work have not been optimized with respect to optical loss, high-order gratings appear promising for future high power laser applications.

To my parents, Paul and Susan Lakomy, who have never stopped believing in me.

ACKNOWLEDGMENTS

I would like to thank my advisor, Professor Kent Choquette, for his many years of guidance, inspiration, knowledge, and support throughout my graduate career. This project would not have been possible without his enthusiastic pursuit to improve the state-of-the-art and patience with me while I am continuously learning and improving. I am grateful to my doctorate committee, Professor J. Gary Eden, Professor Dallesasse, and Professor Minjoo Lee, who have braved a pandemic to give me their much needed advice and research direction. I would like to acknowledge Freedom Photonics, our collaborators on the grant that supported this thesis. Professionally, I am greatly appreciative of the opportunities I have been provided by the IEEE Photonics Society and their encouragement of women in engineering.

I am grateful for the Photonic Device Research Group, who gave me advice on this project and helped me maintain my motivation. Having other students so willing to help me, both senior and junior, is an invaluable asset. I would especially like to recognize the individuals with whom I shared my time at the University of Illinois: Dr. Bradley Thompson, Dr. Zihe Gao, Dr. Harshil Dave, Dr. Stewart Fryslie, Pawel Strzebonski, Raman Kumar, Nusrat Jahan, and William North. You all have inspired and helped me reach an understanding of my research that I never could have achieved alone.

I am fortunate to have been supported for years by the staff at HMNTL. Thank you to those who worked hard and kept things running so I could focus on this degree. The most notable example is the regrowth in this dissertation, which was graciously performed by Dr. Jeongho Park. I would especially like to extend my gratitude to Dane Sievers, whose influence has led to some of the ideas in this dissertation and is constantly inspiring me. This thesis would not have attained

such high quality without Professor Peter Dragic, teaching me about optical bench laser alignment, and Dr. Andrey Mironov, for assisting me with the alternative lithography light source.

I would also like to thank my friends, particularly, Lauren, Dana, John, Myles, Josh, Nicole, Maanav, and Kavita, for their understanding and support of my efforts. Their encouragement and advice enabled me to complete not only this doctorate, but to maintain my sanity as well. I am extremely grateful for my family, who loves and accepts me for who I am. I am blessed to have a family, both immediate and extended, so understanding of my limited communication for years. I would especially like to thank my parents, Paul and Susan Lakomy, for supporting me, motivating me even when I fail, and instilling in me the desire to strive for academic excellence. I feel my success today is due to their love and care throughout my life.

TABLE OF CONTENTS

CHAPTER 1: INTRODUCTION 1

CHAPTER 2: BACKGROUND 6
- 2.1 Distributed Feedback Lasers 6
- 2.2 High Power Distributed Feedback Lasers 9
- 2.3 Lithography Methods 11

CHAPTER 3: THEORY AND SIMULATION 14
- 3.1 Semiconductor Laser Diode Modes 14
- 3.2 Distributed Feedback Lasers 14
- 3.3 Grating Order 15
- 3.4 Coupling Coefficient 16
- 3.5 Effective Distributed Feedback Reflectivity 24
- 3.6 Spectral Envelope 28
- 3.7 Feature Size 31

CHAPTER 4: FABRICATION 37
- 4.1 Broad-Area Edge-Emitting Semiconductor Lasers 37
- 4.2 Surface Grating Lasers 40
- 4.3 Longitudinal Grating Mask 41
- 4.4 Surface-Etched Grating Distributed Feedback Laser Fabrication 42
- 4.5 MOCVD Buried Grating Distributed Feedback Laser Fabrication 47
- 4.6 Laser Facet Coating 51
- 4.7 Alternatives to I-Line Lithography 51

CHAPTER 5: LASER DIODE CHARACTERIZATION 55
- 5.1 Testing Considerations 55
- 5.2 Laser Diode Characterization Setup 56
- 5.3 Surface-Etched Grating Distributed Feedback Laser Characterization 58
- 5.4 Buried Grating Distributed Feedback Laser Characterization 59

CHAPTER 6: CONCLUSIONS AND FUTURE WORK 69
- 6.1 Summary 69
- 6.2 Future Work 71

REFERENCES 73

APPENDIX: EDGE-EMITTING LASER FABRICATION PROCESS 76

CHAPTER 1: INTRODUCTION

Semiconductor diode lasers are optical light sources that have become inseparable from the everyday aspects of modern life, most notably in the way we gather, share, and communicate information. Diode lasers are used to optically transmit the ubiquitous stream of internet data around the globe. Lasers have applications as sensors in digital versatile disc (DVD) players, gas detectors, displays, computers, printers, cell phones and many more consumer devices. Wavelengths of particular importance are 850-920 nm, produced in the AlGaInAs material system on GaAs substrates for short haul communication and optical sensing, and wavelengths in the 1.5 μm regime, created from the InGaAsP material system on InP substrates for long haul communication applications. Diode lasers are also implemented for manufacturing tasks, such as welding, soldering, and optically pumping other (non-semiconductor) laser systems [1]. To meet the demand for high power applications, laser diodes with large gain volume can be made and are often called "broad-area laser diodes" where optimization of efficiency can be critical [2]. For optical pumping applications (e.g. fiber laser excitation), having spectrally narrow laser emission and high power is preferable [3, 4].

This dissertation will focus on approaches for increasing the spectral brightness of broad-area 1550 nm laser diodes using distributed feedback (DFB) gratings, and doing so using fabrication techniques that are inexpensive and suitable for high volume manufacturing. The intended application of these lasers is to serve as an efficient pump source for solid-state and fiber laser systems. The overall spectral efficiency of the pump source can be increased by reducing its lasing emission spectrum to better match the resonance of the media to be excited [4]. One benefit to working with the InGaAsP material system emitting at 1550 nm is the potential to leverage the

laser diode technology that has been optimized for applications in telecommunications, since 1550 nm emission is predominantly used in optical fibers to minimize absorption in silica [5]. However, rather than optimizing the laser design for single mode emission and high speed intensity modulation, as is often the case for telecom lasers, a primary objective of this thesis is promoting high power conversion efficiency at this wavelength and simultaneously increasing the laser diode brightness. An important way to characterize the laser diode beam is by considering the spatial and spectral brightness. Spatial brightness is defined in [6] as the following:

$$Spatial\ Brightness = \frac{Optical\ Power}{\pi^2 * beam\ waist\ radius * half\ angle\ beam\ divergence}.$$

The beam waist is the smallest width of a Gaussian beam, which in the case for laser diodes, is the emission width at the aperture for its lowest-order optical mode. The beam divergence is measured for emission as it leaves the device aperture. Spatial brightness is related to how much power is within the physical beam dimensions per optical mode. The optimal case is for the laser to emit solely into a single fundamental Gaussian mode, which has the lowest beam divergence [6]. Spectral brightness is related to the spectral width of the laser linewidth; distributing the power among multiple optical modes will reduce the laser brightness as compared to the same output power emitted from a single (ideally the fundamental) optical mode. High brightness equates to a laser system with reduced modes to minimize the spectral linewidth while maintaining the same output power. One way to do this is with a surface-etched or buried DFB grating introduced into the device structure [2, 5]. The introduction of a grating is usually meant to control the lasing wavelength, rather than limit the number of lasing modes [2]. However, the introduction of a grating also can increase optical scattering and lead to higher threshold gain. Therefore, to increase brightness, mode reduction using an approach that does not exacerbate the optical loss is necessary.

Broad-area 15xx nm DFB laser diodes with surface-etched and buried gratings are fabricated and characterized in this dissertation for purposes of increasing the laser brightness.

When a DFB structure is implemented within a semiconductor laser, there is an underlying trade-off between efficiency and a narrow spectral linewidth. By limiting the number of oscillating lasing modes, which will narrow the emission spectrum, the maximum output power of a laser may also be diminished. For example, all modes that have sufficient gain will operate, and thus reducing the number of emission modes implies that less of the laser gain spectrum may be accessed. The gain spectrum of the laser diode will move to a longer wavelength range (red-shift) from self-heating. Thus, in the limit of a single allowed longitudinal mode for a DFB laser, when the laser is injected with sufficient carriers, the gain profile no longer spectrally overlaps with this particular longitudinal mode and lasing output will decrease ("roll-over") and eventually cease to lase. For high power laser applications, it is important to maximize the gain volume and to efficiently use the full spectral gain bandwidth. The former led to the development of broad-area edge-emitting lasers with long cavity lengths (typically 2-4 mm) and relatively wide cavity widths (typically ≤ 100 μm). Because of the large gain volume, many optical modes are possible, hence broad-area infrared semiconductor lasers typically have broad (several to 10's of nm) lasing spectral linewidth.

The majority of prior research on DFB edge-emitting lasers has focused on the design and implementation of a one-dimensional photonic crystal (grating) to promote a single longitudinal mode laser emitting at a specific wavelength with narrow spectral width. The objective of this thesis is to explore the middle ground between efficiency and brightness: diode lasers with high power but significantly reduced lasing linewidths. There are several parameters of a grating that can control the "strength" of the DFB effect, which include grating tooth height, order, fill factor,

and the difference between the refractive indices (index contrast) that make up the grating. Grating order (m) is a positive integer that can be selected and used to calculate the resulting grating period from the following expression:

$$\Lambda = \frac{m\lambda_b}{2n_g}, \tag{1}$$

where Λ is the grating period, λ_b is the Bragg wavelength, and n_g is the group refractive index [5]. Grating tooth height and fill factor are discussed at length in Chapter 3. One way to characterize the DFB grating is to determine a parameter called the coupling coefficient. According to Streifer, Scifres, and Burnham's seminal 1975 paper [7], the coupling coefficient "describes the degree to which oppositely going waves transfer energy." The DFB grating periodicity is selected to only permit standing waves with the desired wavelength (Bragg wavelength) to constructively interfere. The coupling coefficient is generally lower for shallow etched, higher-order, and low index contrast gratings [7]. To narrow the lasing spectrum without compromising efficiency, gratings with relatively weaker coupling coefficient will be implemented to minimize the scattering optical loss introduced by the grating structure [8].

To fabricate a DFB grating within a laser diode, the method of transferring the grating pattern to the sample is the manufacturing challenge. For low-order DFB gratings defined for infrared wavelengths, the necessary lithographic resolution ranges from tens to a few hundred nm. Standard i-line contact optical lithography, estimated to have at best 500 nm resolution, cannot meet this resolution requirement. Electron-beam (e-beam) lithography, with an estimated >10 nm resolution, is typically used to achieve the necessary fidelity of the DFB grating pattern [2]. The resolution of direct write e-beam lithography is fundamentally limited by other parameters of the lithography process, such as photoresist choice, development accuracy, and pattern transfer methods, rather than the e-beam itself [9]. As with any type of lithography, the pattern geometry,

such as lines, dots, rectangles as well as proximity effects will affect the resolution. While it is easily capable of meeting the resolution requirements for DFB gratings, e-beam lithography is an expensive and serial manufacturing technique that is beneficial for research applications, but may not be practical for high volume manufacturing [2, 10-12]. E-beam patterning requires a vacuum environment, which is also a disadvantage. The lengthy writing time is further exacerbated by high feature density, which is the case for low-order gratings. In this work, gratings with larger feature sizes that can be fabricated with standard i-line optical lithography are implemented to maintain manufacturability. The alternative of using a shorter wavelength ultra-violet (UV) light source as a substitute for batch exposure is explored. Future experimental fabrication may also benefit from using direct UV laser writing, which is more versatile than i-line lithography [13].

Broad-area 15xx nm DFB laser diodes with gratings are fabricated and characterized in this dissertation for purposes of increasing the laser brightness. In Chapter 2, we review prior research on DFB laser diodes and various device manifestations. In Chapter 3, we investigate and develop a theory to explore the effects of high-order gratings on the resulting laser emission. We show that using high-order gratings with dimensions that are achievable using optical lithography can lead to reduced linewidths, where the facet reflectivities are used in this analysis. The fabrication of diode lasers with surface-etch and epitaxially buried gratings are discussed in detail in Chapter 4. We also show preliminary efforts using UV plasma optical lithography. In Chapter 5, we discuss the experimental characterization of the fabricated broad-area DFB lasers, with particular focus on the buried grating lasers. Finally, we conclude and discuss possible future research in Chapter 6.

CHAPTER 2: BACKGROUND

2.1 Distributed Feedback Lasers

The introduction of periodic refractive index alterations in one dimension within semiconductor laser structures to take advantage of backward Bragg scattering for mode control was first introduced in the 1970s. In 1971, the refractive index of a dye laser medium was periodically altered by Kogelnik and Shank to demonstrate the DFB principle [14]. A few years later, the concept was applied to semiconductor diode lasers, with both single and double heterojunctions, using etched gratings near the active region. The gratings were produced using interference optical lithography and physically etched with ion milling. The subsequent laser structure was then required to undergo a second epitaxial growth step to complete the devices [15, 16]. In 1975, Nakamura *et al.* achieved room temperature continuous wave (CW) laser operation with single longitudinal mode DFB lasers, using a chemically wet etched grating and epitaxial regrowth [17]. The early buried gratings suffered from high losses in the grating region originating from the etching technique and regrowth problems such as interface contamination. The former issue was remedied with the advancement and application of plasma etching techniques, allowing better fidelity, uniformity, and anisotropy than what can be achieved with wet chemical etching. Methods such as in-chamber etch-back steps have been incorporated to reduce interface contamination during epitaxial regrowth [18].

The approaches for introducing a DFB laser grating into a semiconductor diode can be separated into two general categories: either the grating is etched into the surface of the epitaxy (relying on the index difference between the semiconductor and air) or a buried index grating is created within the epitaxial structure by incorporating patterning, etching, and the additional steps

of semiconductor epitaxial regrowth. The regrowth approach enables the grating to be positioned very close to the quantum well active region of the laser, creating a large coupling coefficient. This provides stronger mode control than a surface grating due to greater spatial overlap between the mode and the grating [2] but with reduced index contrast. However, even with the reduced index contrast, buried gratings have the risk of exacerbating the laser diode internal loss, fabrication expense, and complexity [2, 19, 20]. Regrowth methods that require semiconductor exposure to the atmosphere (e.g. for lithography of feature definition) risk the contamination and oxidation of the semiconductor surface on which the regrowth occurs. Regrowth on Al-containing semiconductor surfaces are particularly problematic, since Al oxidizes so readily [2, 21]. Special cleaning procedures, such as chemical cleans and surface etch-backs, are required on the exposed surfaces prior to regrowth [22]. On the other hand, regrowth methods encapsulate the grating surfaces, often eliminate the need for subsequent planarization steps, and dissipate heat more readily than a surface-etched counterpart.

Surface-etched gratings are relatively straightforward to produce and are almost always created using anisotropic dry etching (such as inductively coupled plasma reactive ion etching (ICP/RIE)) to ensure vertical grating side-walls [2]. Since inherently isotropic wet etching produces sloped etched side-walls, this will reduce the pattern fidelity, limit the spatial resolution, and possibly introduce scattering losses to the laser. The strength of the mode control is proportional to the depth of surface-etched gratings and as mentioned previously influences the coupling coefficient of the grating [7]. Deep gratings remove more of the epitaxial material, reducing heat dissipation and introducing more loss, but in turn, provide more mode control [19]. The RIE process inherently possesses so-called "RIE-lag" where the etch rate decreases with decreasing opening size of the feature to be etched [23]. Hence smaller opening sizes can yield a

reduced etch depth. This property can be utilized to create a variation of depths from a single etch, such as the apodized gratings reported in [19] and [24], which exhibit reduced optical scattering loss.

There are a variety of DFB etched gratings that have been previously reported in the literature; these include apodized, high-order, metallic, and side-wall gratings. Apodized (or non-uniform) DFB gratings have been demonstrated that exploit the RIE-lag effect to vary the depth of grating trenches with varying grating tooth width; laser diodes using apodized gratings exhibit maximum powers of a few watts at ~970 nm emission [19]. The benefit of such a design is to reduce the loss from the grating, thereby increasing the slope efficiency of the devices [19, 24]. Higher-order DFB grating lasers have also been shown to provide spectral confinement while increasing the minimum required feature size, enabling less complex and costly lithography [25-28]. Increasing the order of the gratings has also been shown to increase the slope efficiency of the diode laser devices; for example using 135th order gratings in a 975 nm laser achieved a maximum output power of 11 W [25]. Metal surface gratings, such as those fabricated by Kamp *et al*., are not material dependent and can be used for gain coupling, since there is a large imaginary refractive index component in metals. However, metals tend to possess high absorption coefficients and this can be a source of excess optical loss [29]. Another grating-based approach is to add corrugations to the side-walls of a ridge waveguide diode laser. For example, 1550 nm emitting, buried corrugated ridge waveguide diode lasers were demonstrated by Dridi *et al*. to operate with a single longitudinal mode [20]. While common, side-wall DFB gratings are unsuitable for broad-area lasers due to the inherently wide lateral lasing aperture.

The so-called “slotted” laser is another variation of the DFB laser, which implements either grating sections of a small number of periods (<30 is typical) or a series of aperiodic slots, all of

which are intended to reduce the number of lasing modes. The primary application examined with slotted lasers is for high modulation rate optical communication requiring very narrow linewidth with a high side mode suppression ratio (SMSR) [30-32]. Note for communication applications, absolute control of the laser wavelength is a requirement for wavelength division multiplexing (WDM). One notable example is the use of non-uniform high-order slotted surface gratings for such a purpose in [30]. The tunable slotted laser arrays fabricated by Abdullaev *et al*. had grating periods of 8.5 μm or even larger with slot depths of 1.35 μm, boasting single longitudinal mode operation with an SMSR of 50 dB, as well as a lasing threshold below 30 mA. The laser cavities were smaller than 1 mm, which promotes single mode behavior and low threshold, since the longitudinal mode FSR is larger [30]. However, small cavity length results in low power devices, which is reasonable for optical communication, but is not congruent with the objective of this thesis.

2.2 High Power Distributed Feedback Lasers

The general approach to generate high power semiconductor lasers is to maximize the gain volume, which leads to broad-area lasers, but mode control is not pursued [2]. Maintaining high power output and efficiency is a challenge when modifying a laser diode with a DFB structure. In previous work, it has been shown high-order (80th) gratings are preferable for obtaining high efficiency [8, 33]. The particular grating discussed in this report minimizes the amount of loss created by the grating by spacing narrow grooves far apart [33]; in effect a higher-order grating with high fill factor. This grating variety also has the advantage of only requiring standard i-line optical lithography. However, the research in this area has focused on 980 nm lasers in the GaAs-based material system. For this dissertation, the targeted emission wavelength is 15xx nm in the

InP material system. In general, InGaAsP semiconductor materials on InP substrates tend to be much more fragile and have different chemical volatilities, which further complicates laser fabrication.

In addition to adding loss, implementing a DFB grating into a high power laser diode has a profound effect on the effective reflectivity that the laser modes experience. All edge-emitting laser diodes with cleaved facets inherently have confinement in the longitudinal direction arising from the pair of (high refractive index contrast) semiconductor/air interfaces at the facets, which lead to Fabry-Perot longitudinal modes. With the introduction of the grating, we are essentially introducing many additional refractive index interfaces which can constructively contribute "effective" reflectivity. For high power laser diodes, often the facets have high reflectivity (HR) or anti-reflectivity (AR) coatings, in order to have a preferred emission direction.

Equation 2 describes the resonator loss in a Fabry-Perot cavity [2]:

$$\alpha = -\frac{1}{2L}\ln(R_1 R_2), \tag{2}$$

where L is the cavity length with facet reflectivity R_1 and R_2. For a DFB laser, this equation is not sufficient since the grating is not included. Instead, an effective reflectivity can be calculated based on the coupling coefficient (κ) of the DFB grating and used in place of one of the mirror facet reflectivities. According to the analysis of Crump *et al.*, it is desirable for κL (where L is the length of the grating) of a DFB grating to be between 0.1 and 1 [2]. If the κL value is too low, the Fabry-Perot facet reflectivities dominate. On the other hand, if κL is too high, the reflectivity from the DFB grating dominates and reflectivity asymptotically approaches 1 [2]. It has also been reported that enhanced laser efficiency is found when κL is near 0.1 [33]. Note that the reflectivity introduced by the grating dominates the longitudinal cavity confinement if the facets have HR/AR coatings. For high power lasers with uncoated laser facets, the grating reflectivity can be less

significant since the effective reflectivity may be less than the cleaved facet/air interface reflectivity. The impact of the effective grating reflectivity will be further discussed in Chapter 3.

2.3 Lithography Methods

To produce DFB gratings for laser diodes, several methods of lithography have been employed. For gratings with sub-micron sized features, it is standard practice to use e-beam lithography to generate the pattern. E-beam lithography is beneficial for research and prototype development, since it can produce unique, high resolution features. For example, Kamp *et al*. used e-beam lithography to generate first-order DFB gratings with periodicities from 140 to 150 nm [34]. However, as previously mentioned, e-beam lithography is a highly time-intensive, expensive, and most critically, a serial process, where only one laser in a sample can be patterned at a time. Polymethyl methacrylate (PMMA) is a thin resist often used in e-beam lithography and is generally used to reliably pattern features below 10 nm. The cost of direct write e-beam lithography is dependent on the time required to generate the designs, so high feature density can be particularly problematic.

While e-beam lithography is currently the prevalent method for producing DFB gratings, there are other methods for defining the gratings. Interference lithography, sometimes rebranded as holographic lithography, has been utilized to produce DFB gratings for lasers since the 1970s [17]. To generate a grating pattern, two coherent light beams are aligned with optics to form a periodic intensity interference pattern. The periodicity of the generated pattern is determined by the wavelength of light and the spacing/angle of the light sources. Interference lithography cannot achieve the resolution of e-beam lithography, but it can resolve sub-micron features [5]. For example, Schultz *et al*. produced first-order DFB gratings with a 285 nm periodicity with

interference lithography [10]. The greatest drawback of interference lithography is its inability to produce designs of different periodicities with a single exposure. To change the periodicity, the light beams must be recalibrated and additional lithography steps, like masking or applying photoresist, are required [2]. For testing a wide variety of grating designs, producing mixed-order gratings, or aperiodic patterns, this inflexibility is a critical flaw.

DFB laser gratings have also been fabricated using other batch lithography methods that allow for pattern variability. Nano-imprint lithography [2, 35] is a non-wavelength limited lithography technique that relies on specially designed stamps and the application of pressure to transfer designs followed by optical curing. For this process, stamp rigidity and pressure applied are key and must be selected based on the sample size and material. While nano-imprint lithography has been implemented to produce 450 nm pitch DFB gratings, the design considerations are non-trivial and the technique suffers from limited stamp reusability. Note that nano-imprint lithography first requires fabrication of the stamp, which in turn must be patterned, usually by e-beam lithography [2, 35].

Another optical patterning alternative is projection lithography, which uses an optical system of lenses, to reduce the size of the pattern imaged onto the sample. One example of this method for the production of higher-order gratings is reported in [36]. The complex optical system can be used to compensate for aberrations and achieve diffraction limited resolution. The resolution limit of a projection lithography system is generally described by the equation:

$$Resolution = \frac{k_1 \lambda}{NA}, \tag{3}$$

where λ is the operational wavelength, NA is the numerical aperture, and k_1 is a process dependent constant that can be systematically optimized [37]. The maximum value of the numerical aperture is limited by the lenses used in a projection optical system. Since the mask image is reduced several

times for projection lithography, it is necessary for multiple exposures and "stitching together" the image on the sample or wafer. However, the offset between multiple images introduces a stitching error in the lithographic pattern. For patterns that require continuity and are sensitive to slight displacement, like optical gratings, stitching errors can produce fatal flaws [11].

All of the above lithography techniques are capable of achieving better resolution than the (estimated) 500 nm that can be obtained from standard i-line contact lithography [2]. However, there are more factors outside of the lithography method that determine the design resolution. For techniques that use a physical mask for pattern definition, mask positioning, such as achieving close contact with sample (contact lithography) or the relation of the mask with the projection optics, will negatively influence the obtained resolution. Sample flatness and source uniformity are imperative to maintaining consistency in any lithographic process. In addition, the photoresist used to transfer lithography patterns has its own resolution limit and thickness considerations. Experimental factors, such as exposure and development time of the photoresist, will also negatively contribute to resolution. For the fabrication portion of this thesis, we choose the minimum feature sizes of the gratings such that standard i-line optical lithography can be used. This necessarily requires the design of higher-order gratings. However, the alternative optical lithography methods for grating definition such as vacuum ultra-violet (VUV) plasma lithography and direct UV laser writing will be addressed in Chapter 4.

CHAPTER 3: THEORY AND SIMULATION

3.1 Semiconductor Laser Diode Modes

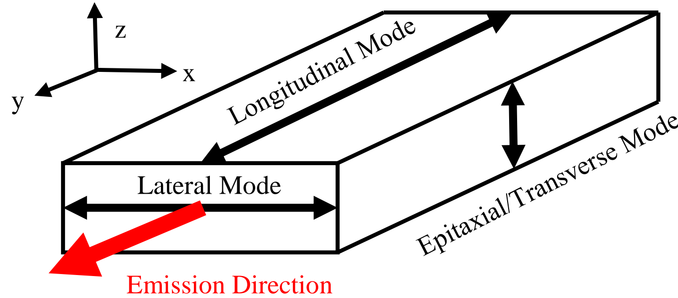

Figure 1: Mode orientations in an edge-emitting laser showing the longitudinal, lateral, and transverse modes.

There are three types of modes in an edge-emitting semiconductor diode laser, such as shown in Figure 1: longitudinal, lateral, and transverse modes. Longitudinal modes are in the direction of light propagation (y-direction in Figure 1) and are determined by the cavity length. Which longitudinal modes oscillate is determined by their spectral overlap with the gain spectrum [5]. Transverse modes are influenced by the refractive indices of the epitaxial layers in the z-direction in Figure 1, and thus can be called epitaxial modes. Lateral modes are in the third direction (x-direction in Figure 1) and are influenced by the laser fabrication method. In this dissertation, the focus will be to control and reduce the number of longitudinal modes propagating in edge-emitting lasers using a DFB structure either etched into the surface of the laser or a patterned and buried via regrowth within the epitaxy.

3.2 Distributed Feedback Lasers

Rather than having a uniform gain region of a broad-area laser, the DFB laser “distributes” the optical gain periodically along the propagation direction of the laser. The purpose of this is to

enhance the coupling between the forward and reverse propagating waves of a specific wavelength thereby ideally selecting a single longitudinal mode to lase. A straightforward manner of creating the desired periodicity is to introduce a refractive index grating in or near the gain region so that the laser mode, which interacts with the grating, is amplified [5].

3.3 Grating Order

In this thesis, the purpose of a DFB grating is to reduce the number of propagating modes in a laser to achieve a narrower spectral linewidth. The periodic grating limits the number of modes by introducing refractive index perturbations, which create additional reflection boundaries along the longitudinal laser direction. However, the grating should also not introduce excessive optical loss from these additional refractive index interfaces. If nearly the same output power from a broad-area laser can be achieved in a design with fewer longitudinal modes oscillating, the emission brightness will increase.

When a plane wave of light propagating in a medium, A, encounters a boundary with another medium, B, at normal incidence, a portion of the light is transmitted into medium B and the rest is reflected back into medium A. How much light power is reflected is determined from the refractive index difference between mediums A (index n_A) and B (index n_B):

$$Reflectivity\ (\%) = \left(\frac{n_A - n_B}{n_A + n_B}\right)^2. \qquad (4)$$

The larger the index difference (or contrast), the more light power reflected at the interface. Since DFB gratings rely on periodic reflectivity, the strength of the grating influence is strongly dependent on the refractive index difference between the two materials that make up the grating. The overlap of the grating with the epitaxial mode will also influence the strength of the grating, thus the position of the grating with the epitaxial mode in the cavity is also a design parameter.

For reflected light, propagating in the same direction, to interfere constructively, the phase between the waves must be a multiple of 2π. Thus, for a mode to constructively interfere and propagate through a grating it must satisfy the Bragg condition in Equation (1). Modes that satisfy the Bragg condition experience more gain and become dominant over other modes if the spectral overlap with the gain spectrum is sufficient. For an edge-emitting laser with many longitudinal modes, DFB gratings provide a mechanism to select a few to a single longitudinal mode. The periodicity of the grating is determined from the Bragg condition for the desired lasing wavelength, grating order, and material [5].

In order to fabricate a DFB it is imperative to consider the practicality of resolving the grating features. Using Equation (1), a first-order grating for a 1.55 μm laser (InGaAsP, $n_g = 3.4$) will have a periodicity of 0.23 μm, which requires lithographic resolution not achievable with standard i-line contact lithography [5]. One way to circumvent this issue is to use a higher order of the grating. Prior research of high-order DFB gratings [28], cite the expense of e-beam lithography as the motivation for implementing high-order gratings. Higher-order gratings dramatically relax the resolution constraint on fabrication but allow more wavelengths to satisfy to phase condition. As demonstrated by Fricke *et al*. [25], increasing grating order can lead to higher device efficiency and power output, but less single longitudinal mode behavior.

3.4 Coupling Coefficient

The coupling coefficient, κ, which can be a complex parameter, is used to characterize DFB gratings throughout the literature [2, 5]. The coupling coefficient, which describes the strength of the interaction and the degree of feedback in the grating structure, is numerically extracted from experimental data or computationally modeled. It takes into account the coupling

between the forward and reverse propagating waves to determine what conditions yield constructive interference. The coupling coefficient is proportional to the variation of the refractive index step and the number of corrugations per length in the grating [38]. As defined, the coupling coefficient should be nonzero and positive. A zero or negative coupling coefficient indicates a wave that cannot satisfy the standing wave condition or is evanescent, respectively. Rather than evaluating the coupling coefficient directly, a common practice is consider the product of the coupling coefficient with the overall grating length. This product can then be used to calculate the expected grating reflectivity and absorption [2].

The following discussion is derived from coupled mode theory. The coupling coefficient depends on the geometry of the grating, grating tooth height, Bragg order, material refractive indices, and the overlap of the grating with the laser cavity mode. For our model we assume the purely index coupled case, meaning the coupling coefficient is real (a benefit for the successful the convergence of the imbedded transcendental equations) [5, 7]. The coupling coefficient monotonically increases with grating tooth height and with higher refractive index contrast, regardless of the grating geometry [7]. The coupling coefficient also decreases as the overlap between the grating and transverse mode is reduced, by positioning the grating within the cavity where the light intensity is weaker [10].

The relationship between Bragg order and the coupling coefficient is a bit more complicated. Streifer *et al.* analyzed the coupling coefficient for buried rectangular DFB gratings and reports a calculation for low Bragg orders. We adopt this analysis as a starting point for an approximate model for the buried gratings to be pursued in this work. We then extend this analysis to high-order gratings to investigate the effect of larger orders on the coupling coefficient using

appropriate material parameters for our laser structure. From coupled mode theory for the grating geometry in Figure 2, the coupling coefficient can be described by [7]:

$$\kappa = \frac{k_0^2}{2\beta N^2} \int index\ perturbation * E^2(x)dx, \qquad (5)$$

where $k_0 = \frac{2\pi}{\lambda_0}$, and the variables in Equation (5) are defined in Table 1. The model sketched in Figure 2a) consists of two cladding layers (Region 1 and Region 3) surrounding a high index core region (Region 2). The thickness t, t', regional refractive indices, and grating period are also represented in Figure 2a). The buried grating in the structure is between Region 1 and Region 2 with the origin chosen to be at the center of the grating tooth height, as depicted by the dotted lines in Figure 2a) and b). Since Region 2 has a relative high index, the fill factor, defined in Table 1 represents the percentage of the material that has not been etched away. Note that the fill factor definition holds for both surface and buried gratings. The (blue) shaded regions in Figure 2b) denote areas, A and B, above and below the origin. The index perturbation, in Equation (5) is the piecewise description of the index difference as a function of x and z. For the x, z coordinates in area A, including those periodically identical, the index perturbation is $n_1^2 - n_2^2$. Similarly, the x, z coordinates within areas periodically identical to area B have an index perturbation equivalent to $n_2^2 - n_1^2$ [7].

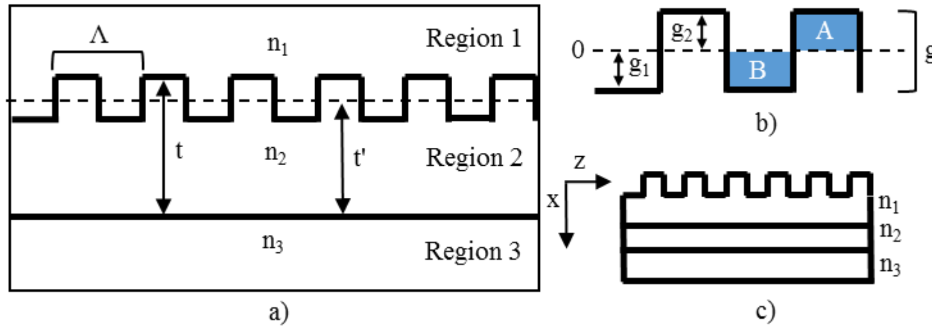

Figure 2: Buried grating laser model structure for calculating the coupling coefficient. Adapted from [7]: a) laser cross-section of model, b) enlarged view of grating section, and c) cross-section of surface grating laser.

Table 1: Coupling Coefficient Calculation Variables

Variable	Description
κ	Coupling coefficient
N^2	Normalization constant
$E(x)$	Electric field
$\frac{w}{\Lambda}$	Fill factor
t	Core thickness
t'	Core thickness below origin
n_1, n_2, n_3	Refractive index of Regions 1, 2, and 3, respectively
k_0	Wave number in free space
β	Propagation constant
g	Total grating tooth height
g_1, g_2	Grating tooth height above and below the origin, respectively
m	Bragg order

The motivation for adopting this model is to qualitatively estimate with relative simplicity, the coupling coefficient for both surface and buried grating lasers. The surface grating lasers discussed in Chapter 4 have a layout such as the configuration shown in Figure 2c), while the buried grating lasers more closely resemble the structure in Figure 2a). The buried grating design used in this work has the grating positioned within the cladding rather than in the core as depicted in Figure 2a). To use this model for offset gratings, both etched into the surface and epitaxially buried within the laser cavity, we use an "effective" grating tooth height in the model to account for the differences in the grating structures.

Note for the DFB lasers characterized in this work, the coupling coefficient calculated in the model represents an upper bound for the gratings, since the overlap of the transverse modes in

the cavity with surface-etched grating or an/offset buried grating are both is less than a buried grating bordering the active region, see the mode approximation below. Thus, we use Equation (5) to establish the trends of the coupling coefficient and for the various grating structures, while recognizing the values are an upper bound. The electric field for the laser emission in the buried grating model shown in Figure 2 is defined as [7]:

$$E(x) = \begin{cases} e^{qx}, \quad x \leq 0 \\ \cos(hx) + \frac{q}{h}\sin(hx), \ 0 \leq x \leq t' \\ e^{-p(x-t')}\left(\cos(ht') + \frac{q}{h}\sin(ht')\right), \ t' \leq x \end{cases} \tag{6}$$

and

$$q = \sqrt{\beta^2 - n_1^2 k_0}, \ h = \sqrt{n_2^2 k_0 - \beta^2}, \ p = \sqrt{\beta^2 - n_3^2 k_0}. \tag{7}$$

The value of t' is determined by the location of the chosen of origin in Figure 2, which is selected so the area of the grating in Region 1 is the same as that in Region 2, as shown in Figure 2a) and 2b). In Equations (6) and (7), the propagation constant can be determined using the waveguide transcendental equation [7]:

$$\tan(ht') = \frac{h(q+p)}{h^2 - pq}. \tag{8}$$

The overlap of the electric field of the mode with the grating determines the impact of the grating position within the laser waveguide. If the grating is moved away from the epitaxial mode center, such as for the case of a surface grating, the mode overlap decreases along with the coupling coefficient. The mode normalization constant can be solved using [7]:

$$N^2 = \int_{-\infty}^{\infty} E^2(x)dx = \frac{(h^2+q^2)(t'+\frac{1}{q}+\frac{1}{p})}{2h^2}. \tag{9}$$

Incorporating the refractive index perturbation of the rectangular grating case and solving the integral in Equation (5), the coupling coefficient becomes [7]:

$$\kappa = \frac{k_0^2(n_1^2-n_2^2)}{4\pi\beta m N^2} \sin\left(\frac{\pi m w}{\Lambda}\right) \left[g_2 + \sin\left(\frac{2g_2 h}{2h}\right) + \frac{q}{h^2}(1-\cos(2g_2 h)) + \frac{q^2}{h^2}\left(g_2 - \frac{\sin(2g_2 h)}{2h}\right) + \frac{1}{q}(1-e^{-2g_1 q})\right]. \quad (10)$$

Using Equation (10) with the appropriate experimental parameters for refractive indices at 1.55 μm wavelength, 50% grating fill factor, and core thickness, yields the solutions for the rectangular grating coupling coefficient as a function of Bragg order and grating depth as plotted in Figure 3. Figure 3 shows the coupling coefficient monotonically increases with effective grating tooth height [7].

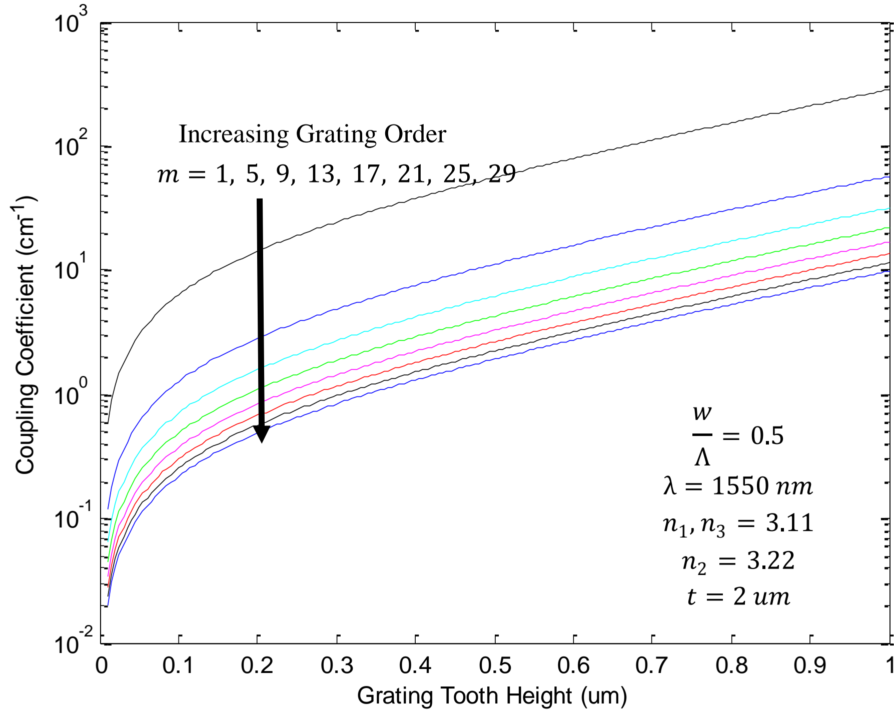

Figure 3: Calculated coupling coefficient using the model of Striefer *et al*. [7], for the rectangular DFB grating case as a function of grating depth (x-axis) and Bragg order (m). The grating orders below 29 that do not yield a valid solution are not included.

However, not all grating order/fill factor combinations are valid. Consider the sine term in the overall multiplication factor in the coupling coefficient Equation (10). If $\frac{mw}{\Lambda}$ becomes an integer, the coupling coefficient vanishes. Also, if $\sin(\frac{\pi m w}{\Lambda}) < 0$, this produces a negative

coupling coefficient. A zero or negative coupling coefficient signifies a non-propagating or unsustainable condition, and the corresponding Bragg order and fill factor pair do not permit a proper DFB grating. Therefore, the valid grating orders will fluctuate based on the fill factor of the

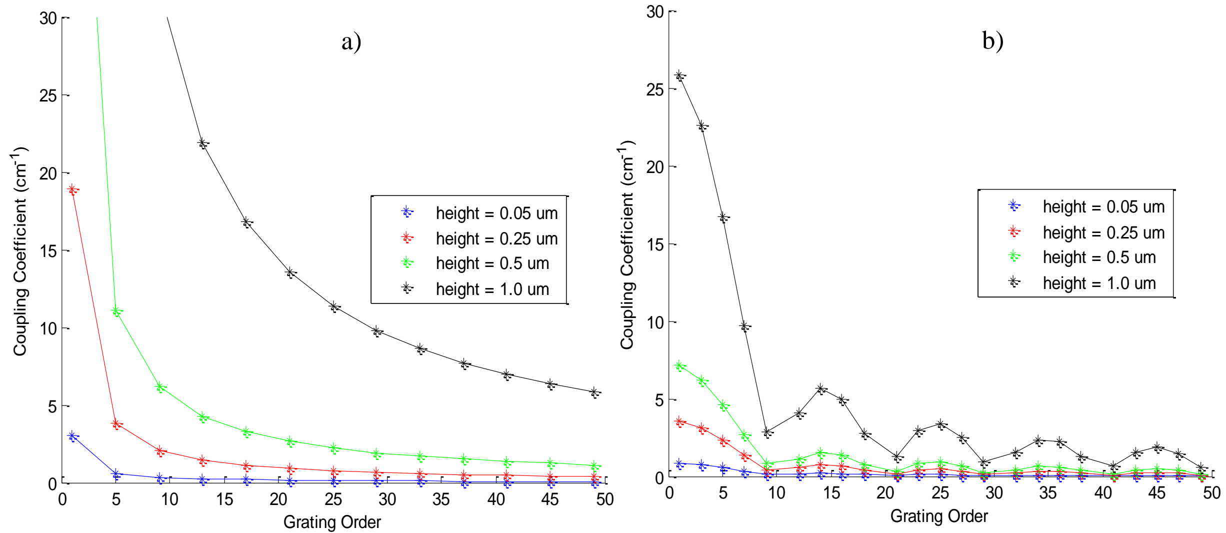

Figure 4: The coupling coefficient calculated for the rectangular DFB grating with: a) 50% fill factor and b) 90% fill factor. The valid grating orders are denoted with points, while the curves are simply a guide for the eye.

grating. Figure 4 shows the coupling coefficient calculated for 50% and 90% fill factor gratings as a function of grating order. The difference in coupling coefficient between the two sets is directly caused by the fluctuation in the sine term of Equation (10). For all valid grating orders, the 50% fill factor gratings in Figure 4a) have $\sin\left(\frac{\pi m w}{\Lambda}\right) = 1$, the maximum value for the multiplicative term, creating a monotonically decreasing coupling coefficient with increasing grating order. On the other hand, the 90% fill factor gratings experience periodic oscillation from $\sin\left(\frac{\pi m w}{\Lambda}\right)$, allowing local maximums in the coupling coefficient. Note, the coupling coefficient for a given grating height in Figure 4a) is consistently higher than that obtained in Figure 4b). It has been also been suggested that surface gratings with high fill factor have a lower optical scattering loss penalty [8, 33].

To account for the different position of the grating relative to the Gaussian transverse mode, the effective grating height parameter is used. To approximately calibrate the grating tooth height in the parameter model and we can compare a fabricated first-order DFB grating laser fabricated by Freedom Photonics using identical epitaxial wafers. This DFB laser has a geometrically estimated coupling coefficient of 2.99 cm^{-1} for the first-order, 200 nm tooth height, buried DFB grating. From our model using Figure 3, a grating tooth height of 50 nm corresponds to a 2.99 cm^{-1} coupling coefficient. The actual grating tooth height is 200 nm, but the grating is located in the cladding with less of the structure overlapping the optical mode. Using this grating height equivalency, Figure 5 specifically estimates the effect of grating order on the coupling coefficient for DFB lasers with the same grating location and tooth height. In the literature, typical DFB lasers are reported with grating coupling coefficients within the same order of magnitude [10, 20, 26, 27]. However, the coupling coefficient estimates beyond the first few valid grating orders in Figure 5 are relatively small.

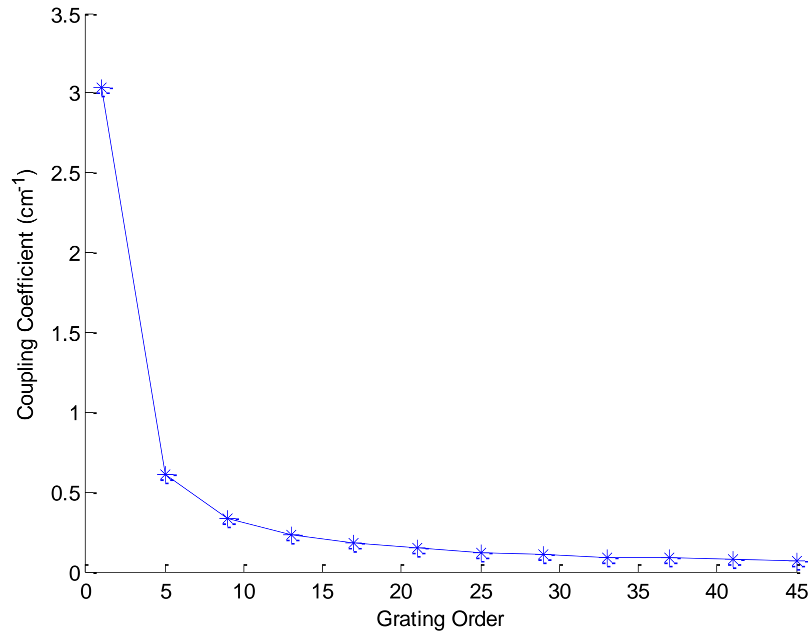

Figure 5: Calibrated coupling coefficient calculated for the rectangular DFB grating with an equivalent height of 50 nm and a fill factor of 50%. The valid grating orders are denoted with points, while the curve is a guide for the eye.

3.5 Effective Distributed Feedback Reflectivity

As discussed in Chapter 2, DFB gratings can dramatically influence the effective reflectivity of the laser cavity. It is possible to calculate the additional reflectivity introduced by a DFB grating using the coupling coefficient [2]. Determining the effective reflectivity can help predict the behavior of the DFB grating laser by estimating how much the resonator loss is expected to change. The following analysis is adapted from the combination of Crump *et al.* [2] as well as Zheng and Taylor [39].

We begin with Equation (2), which determines mirror loss in a Fabry-Perot cavity. In order to apply this equation to the case of the DFB laser, we can use the total resonator loss, α_r and set it equal to Equation (2). Ultimately, the effective reflectivity can be solved for given the initial facet reflectivities. The resonator loss has been determined by Zheng and Taylor [39] using coupled mode analysis in extensive detail for a variety of cases. For this work, the resulting solutions will be described as well as the assumptions taken from Zheng and Taylor.

The resonator loss, ignoring the imaginary component, is calculated for two distinct cases: (i) a laser with coated facets, and (ii) a laser with uncoated facets. The former assumes that the approximation of no facet reflectivities ($r_0 = 0$) is valid, since r_0 is obtained from:

$$r_0 = \sqrt{R_1 R_2} \tag{11}$$

and when one facet reflectivity is 1 and the other is very small, r_0 approaches the purely DFB case. The terms for resonator loss (g) and the propagation constant (γ) contain both real and imaginary parts. The real part of the resonator loss, g_r, can be analytically solved for in terms of κL. For the $r_0 = 0$ case the following coupled equations are used to determine g_r:

$$g_r L = \gamma_r L - \kappa L e^{-\gamma_r L} \sin(\gamma_i L) \tag{12}$$

$$\gamma_r L = \frac{1}{2}\kappa L\left(e^{-\gamma_r L} + e^{\gamma_r L}\right)\sin(\gamma_i L) \tag{13}$$

$$\gamma_i L = \frac{1}{2}\kappa L(e^{-\gamma_r L} - e^{\gamma_r L})\cos(\gamma_i L), \tag{14}$$

where γ_r and γ_i are the real and complex parts of the propagation constant from the wave equations. These transcendental equations are solved numerically in terms of κL without additional approximations [39]. Combining this solution with Equation (2), an effective reflectivity, R_{eff}, can be calculated from $g_r L = -\frac{1}{2}\ln(R_1 R_{eff})$, which for one perfect reflective facet ($R_1 = 1$) simplifies to:

$$R_{eff} = e^{-2g_r L}. \tag{15}$$

For the uncoated laser case, $r_0 \neq 0$ and thus the equations to numerically determine the resonator loss increase in complexity. Using a refractive index of 3.22 for InP, the uncoated facet reflectivity is calculated from Equation (4) to be ~0.28. Since both facets have the identical $r_0 = 0.28$, the effective reflectivity equation becomes:

$$R_{eff} = e^{-g_r L}. \tag{16}$$

The solution for the resonator loss begins with the following relationship between the coupling coefficient and the resonator loss [39]:

$$-ja_0\kappa = (-g + \gamma + j\delta)e^{-j\Omega}e^{L(\gamma + j\delta)}, \tag{17}$$

where

$$a_0 = \frac{r_0 e^{L(\gamma + j\delta)} - e^{j\Omega}}{e^{j\Omega} - r_0 e^{L(-\gamma + j\delta)}}. \tag{18}$$

The phase contribution is included using δ as the detuning factor and Ω as the residual phase. For this calculation the phase contribution will be ignored, and thus $\delta = 0$ and $\Omega = 0$. Equations (17) and (18) simplify to:

$$-j\left(\frac{r_0 e^{\gamma L} - 1}{1 - r_0 e^{-\gamma L}}\right)\kappa = (-g + \gamma)e^{\gamma L}. \tag{19}$$

Equation 19 is multiplied by L and separated into real and imaginary parts, which yields:

$$j\frac{r_0 e^{\gamma_r L + j\gamma_i L} - 1}{e^{\gamma_r L + j\gamma_i L} - r_o}\kappa L + \gamma_r L + j\gamma_i L = gL. \tag{20}$$

We only need the real part of the propagation constant, the exponential terms with imaginary and real components are separated with Euler's formula into trigonometric functions. The resulting complex denominator is multiplied by the complex conjugate and simplified to isolate just the real component of g_r:

$$\frac{(r_0^2 - 1)e^{\gamma_r L} sin(\gamma_i L)}{e^{2\gamma_r L} - 2r_o e^{\gamma_r L}\cos(\gamma_i L) + r_0^2}\kappa L + \gamma_r L = g_r L. \tag{21}$$

Since $r_0 \neq 0$, the propagation constant is determined numerically from the following coupled transcendental equations [39]:

$$\gamma_r = \frac{p\kappa}{2m}\left(\frac{m^2}{p^2 + q^2} + 1\right) \tag{22}$$

$$\gamma_i = \frac{p\kappa}{2m}\left(\frac{m^2}{p^2 + q^2} - 1\right), \tag{23}$$

where

$$p = (1 - r_0^2)e^{\gamma_r L}\sin(\gamma_i L) \tag{24}$$

$$q = -(1 + r_0^2)e^{\gamma_r L}\cos(\gamma_i L) + r_0(1 + e^{2\gamma_r L}) \tag{25}$$

$$m = e^{2\gamma_r L} + r_0^2 - 2r_0\cos(\gamma_i L). \tag{26}$$

The effective reflectivity is plotted as a function of grating order for 50% fill factor gratings in Figure 6 and 90% fill factor gratings in Figure 7. The effective reflectivities in Figures 6 and 7 are shown for both uncoated and coated facets and are calculated for 2 mm laser cavity length devices. It is seen from both figures that the effective reflectivity decreases rapidly with grating order. In both figures, the uncoated reflectivity saturates to the native facet reflectivity value of ~28%, whereas the coated laser effective reflectivity saturates to zero with increasing grating order. The range for the effective reflectivity is larger for the coated lasers particularly the 50% fill factor gratings, which shows how facet coating is a valid way to add more flexibility to the

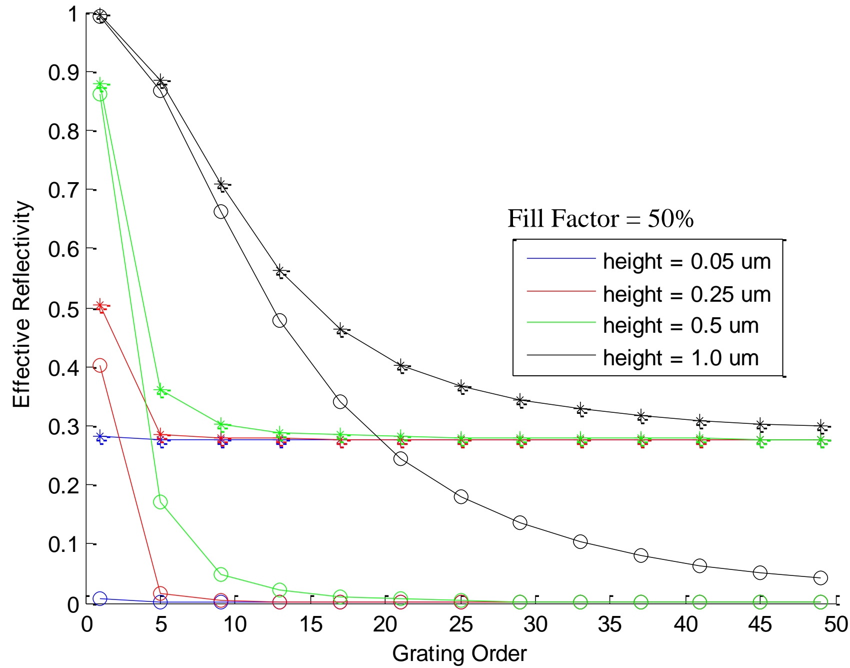

Figure 6: Calculated effective facet reflectivity for 50% fill factor and effective grating tooth heights. The star points are for uncoated facets, while open circles are for coated laser facets. The valid grating orders are denoted with points, while the curves are guides for the eye.

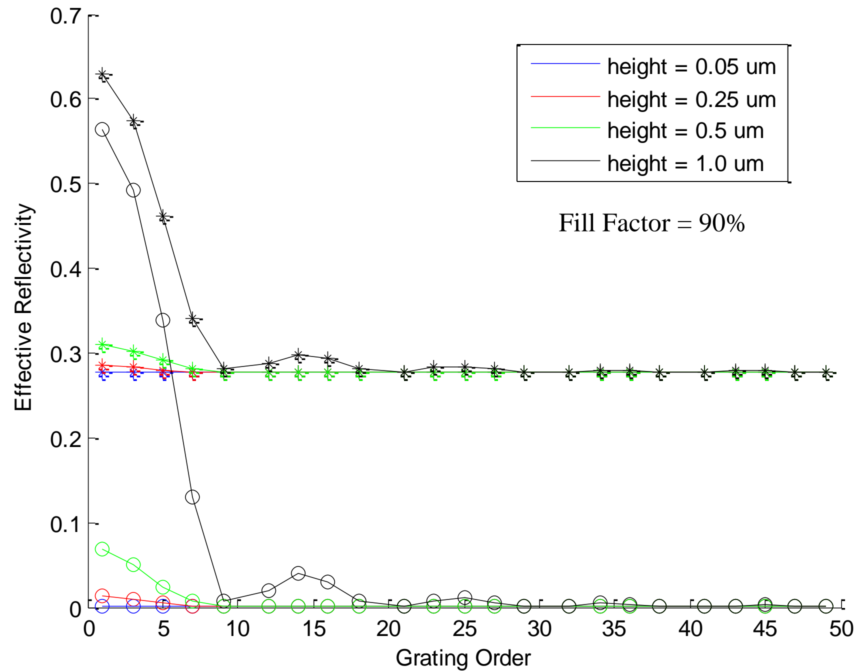

Figure 7: Calculated effective facet reflectivity for 90% fill factor and effective grating tooth heights. The star points are for uncoated facets, while open circles are for coated laser facets. The valid grating orders are denoted with points, while the curves are guides for the eye.

DFB design. For 50% fill factor gratings in Figure 6, the smaller grating order effective reflectivity

is dominated by the influence of the DFB grating, since the coupling coefficient is so high. However, this is less the case for the 90% fill factor gratings in Figure 7, since the coupling coefficient is substantially lower and approaches the inherent asymptotes at a lower grating orders. The coated facet curves in Figure 6 corresponding to a 50 nm effective height, correlates to the Freedom Photonics first-order DFB laser. For this case, Figure 6 suggests the change in effective reflectivity imparted from the grating is extremely low.

A final comment regarding the difference between coated and uncoated lasers is the round trip phase requirement. Note that the location of the cleaved facet is controlled no better than within 50 μm, and thus the termination location of the DFB grating is random. For uncoated lasers it is likely both facets are not optimally aligned with the grating, while for a coated laser only the high-reflection facet is a concern. Due to the strong pinning of the phase by the facet, both variations in the lasing wavelength and effective reflectivity are expected due to the facet cleave location uncertainty [2]. Therefore the reflectivity estimates in Figures 6 and 7 represent the best case and are upper bounds.

3.6 Spectral Envelope

Streifer *et al.* [40] present a reflectance dependent model to estimate of the spectral envelope expected from the laser diode emission. The effective DFB reflectivity determined in the previous section can be used as input into this model to predict the effect of DFB gratings on the spectral linewidth of DFB lasers. The model only considers a single transverse electric (TE) mode, lasers under CW operation, and spectral inhomogeneity is ignored. There is also nonlinear dependence on parameters that can only be determined experimentally. For application in this

work, the spectral full width at half maximum (FWHM) linewidth is normalized to the spontaneous emission linewidth to enable comparison between grating orders.

From this model the following equations can be used [40]:

$$\lambda_{FWHM} = \lambda_h \left(\frac{P_t}{\sqrt{4P_s^2+1}} - \frac{P_t}{2P_s} \right) \tag{27}$$

$$P_s = \left(\frac{(1-R_1)(\sqrt{R_1}+\sqrt{R_2})(1-\sqrt{R_1 R_2})}{-2R_1\sqrt{R_2}\ln(R_1 R_2)} \right) \frac{hc\lambda_o K}{4\pi n_a n_e A}, \tag{28}$$

where λ_{FWHM}, P_t, λ_h, λ_0, n_a, n_e, h, c, R_1, and R_2 are the spectral envelope FWHM, power transmitted, homogenous spontaneous linewidth, free-space emission wavelength, active region refractive index, modal refractive index, Planck's constant, the speed of light, the facet reflectivities, respectively. In Equation (28), A is calculated from material parameters and taken to be 6 x 10^{-25} cm^2 s, as determined in [40]. K, the spontaneous emission factor, is set to one [40]. For the both the coated ($R_2 = 1$) and uncoated ($R_2 = R_1$) laser cases, Equation (28) simplifies to:

$$P_s = \left(\frac{(1-R_1)^2}{-2R_1 \ln(R_1)} \right) \frac{hc\lambda_o K}{4\pi n_a n_e A}. \tag{29}$$

Figures 8 and 9 show the estimated emission linewidth for coated and uncoated facets as a function of grating order for 50% and 90% fill factor gratings, respectively. For these figures the other parameters needed in Equations (28) and (29) are set as follows: $P_t = 2$ mW, $\lambda_h =$ 1 nm, $\lambda_0 = 1550$ nm, $n_a = 3.22$, $n_e = 3.20$ throughout the spectral linewidth calculation. The absolute numerical values obtained using this method are scaled by experimentally measured

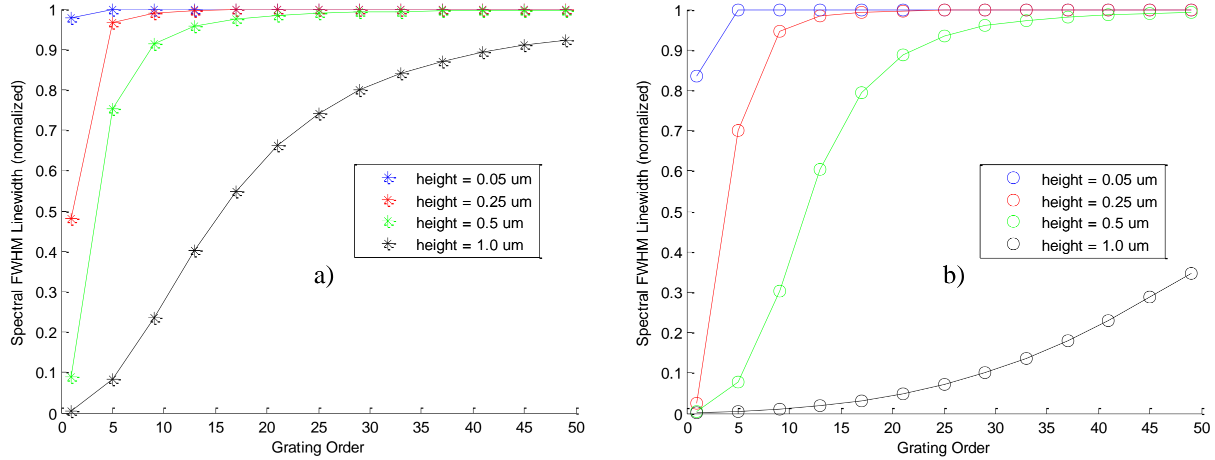

Figure 8: Normalized spectral FWHM as a function of grating order and grating tooth height with 50% fill factor for: a) uncoated laser facets and b) coated laser facets.

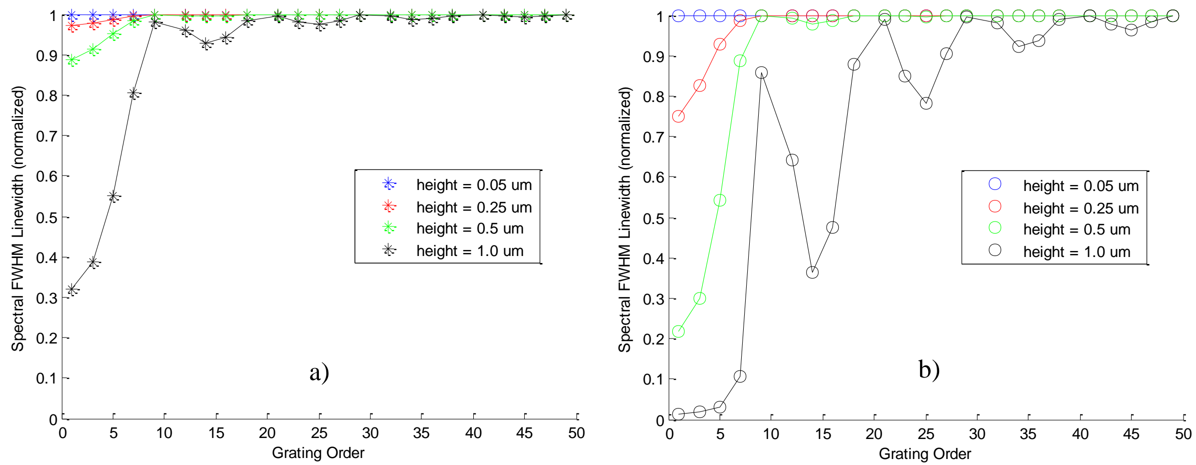

Figure 9: Normalized spectral FWHM linewidth as a function of grating order and grating tooth height with 90% fill factor for: a) uncoated laser facets and b) coated laser facets.

parameters. Thus, the homogenous spontaneous linewidth in Figures 8 and 9 are normalized to the threshold linewidth of the control laser diodes without gratings to illustrate how the spectral linewidth will deviate.

In Figures 8 and 9, the first-order gratings show the greatest reduction of linewidth, as expected for single longitudinal mode lasers. Generally, for increasing grating order, the emission linewidth rapidly converges to the wide spectral emission of the broad-area laser. However, as coupling coefficient is increased, (e.g. increased grating height) reduction of the spectral linewidth is observed. However, this trend is overshadowed by the effect of the laser coating. DFB gratings

implemented for coated lasers show far more spectral reduction than uncoated laser DFB gratings, despite having the same coupling coefficient. The effect of the coating is so dramatic that DFB gratings for uncoated laser should be designed and optimized separately.

As predicted from the coupling coefficient, the grating tooth height has a substantial effect on how much the spectral linewidth is expected to change compared to devices without gratings. Specifically, the 0.05 μm grating height in Figures 8 and 9 predict virtually no spectral difference at higher grating order, because the grating strength is too low. Since the coupling coefficient used in this set of calculations is already an upper bound, the spectral linewidth reduction should be less than what is predicted by the model. On the other hand, the model can be used to eliminate designs with gratings that are too weak.

The oscillation behavior of the coupling coefficient for the 90% fill factor case, apparent in Figure 7, is also observed in the spectral linewidth estimate, producing local minima and maxima, especially for the case of uncoated laser facets in Figure 9b). Notice the local minima in the linewidths can be used to select higher grating orders that will still produce strong spectral reduction. With different fill factors, the local minima occur at different grating orders. With constant fill factor, higher grating orders become easier to lithographically define since the grating feature size is larger.

3.7 Feature Size

In order to successfully implement a DFB grating, the lithography resolution must be sufficiently small to achieve feature definition. Thus, the lithography method used to define the gratings, sets the limit for how small the feature size can be. Minimum grating feature size is a function of both grating order and fill factor, as illustrated by the contour plot in Figure 10. Note

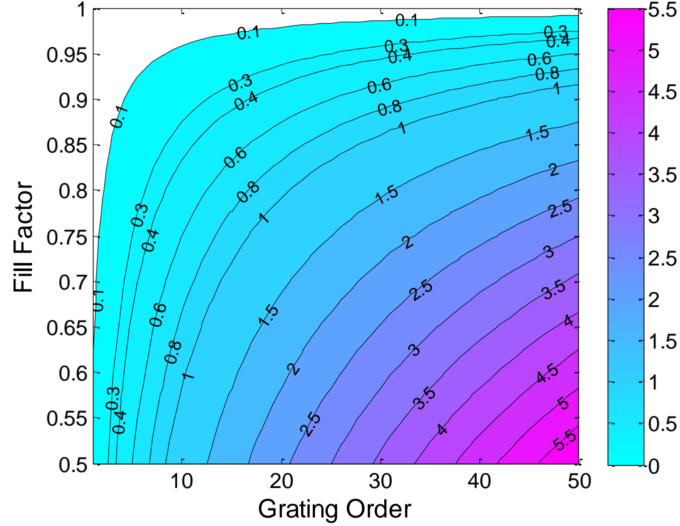

Figure 10: The minimum feature size (color axis and denoted on contours) in microns as a function of grating order and fill factor.

the smallest submicron feature contour in Figure 10 implies that the small features can be used for low order/small fill factor designs or high-order/high fill factor designs, where the latter designs are also expected to have reduced optical scattering [8, 33]. Therefore, the coupling coefficient, effective reflectivity, and spectral linewidth calculations in the previous sections, can all be expressed in terms of minimum feature size instead of grating order, by referencing Figure 10. The minimum feature size considered here is 300 nm, since preliminary experiments have indicated this resolution is consistently achievable with direct laser writing lithography [41]. Fill factors less than 50% are not considered, since the feature size is maximum at 50% and it has been shown that etched narrow trench features are preferred for high power laser efficiency [2, 24]. For fill factors greater than 50%, the minimum feature size essentially describes the width of the etched trench features.

By varying the fill factor, a 300 nm feature size can be selected for each grating order, higher than the 3rd order, which is equivalent to designs along the 300 nm contour line in Figure 10. The calculations described earlier in this chapter for coupling coefficient, effective reflectivity, and the estimated linewidth are repeated for a 300 nm minimum features size and are displayed in

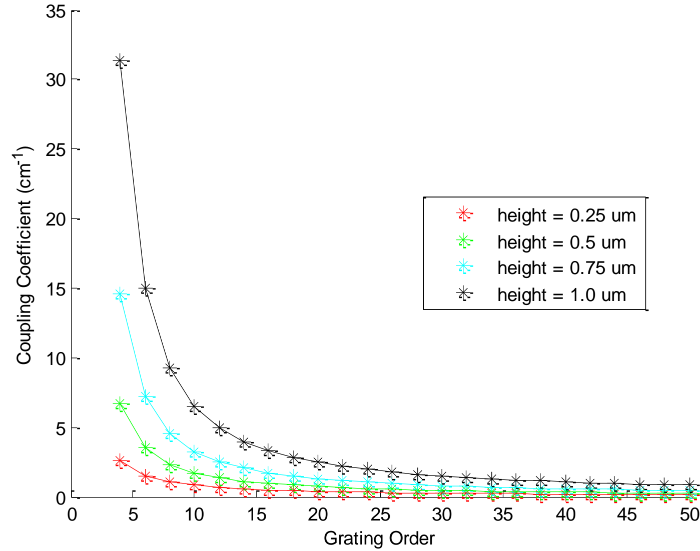

Figure 11: Coupling coefficient calculated for 300 nm minimum feature size gratings. The fill factor is varied to yield the desired feature size for each grating order. The effective heights used in the calculation are denoted by different colors. The valid grating orders are denoted with markers and connected with a line to guide the eye.

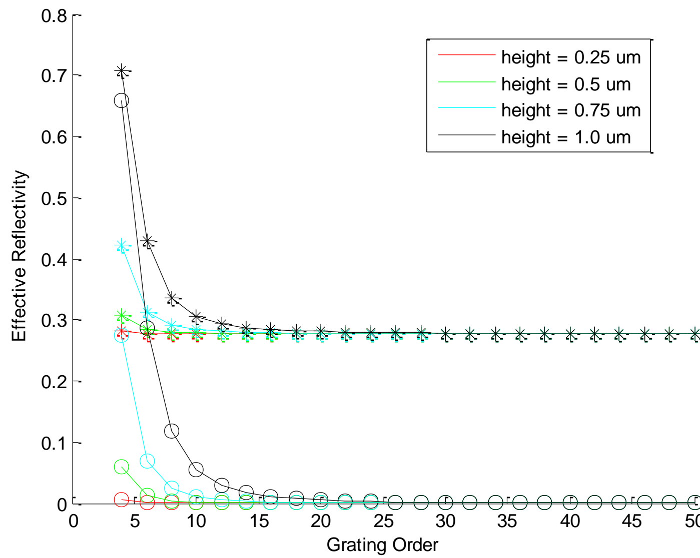

Figure 12: Effective facet reflectivity for 300 nm minimum feature size gratings. The star points are for uncoated facets, while the open circles are for coated laser facets. The valid grating orders are denoted with points, while the curves are guides for the eye.

Figures 11, 12, and 13, respectively. It can be seen that for uncoated/coated lasers, the grating orders higher than the $10^{th}/18^{th}$ (lower for smaller grating tooth heights) show insufficient linewidth narrowing and thus are not worth pursuing. Since the fill factor varies in these figures, which grating orders are valid differs from the previous cases examined. For instance, in the 50% fill factor case, about ¼ of the grating orders produce a result that supports the standing wave

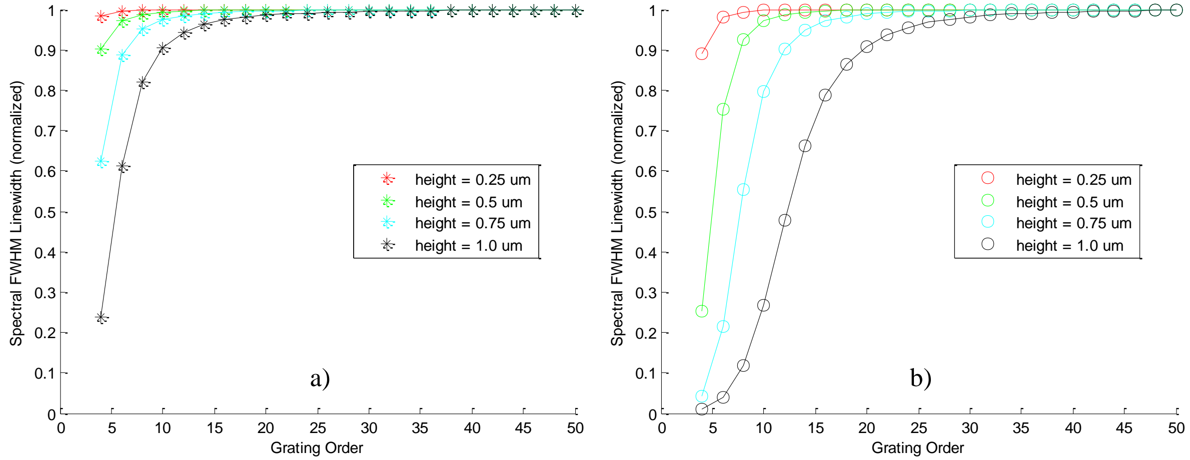

Figure 13: Normalized spectral FWHM linewidth as a function of grating order and grating tooth height for gratings with 300 nm minimum feature size. The fill factor is varied to yield the desired feature size for each grating order for the following: a) uncoated laser facets and b) coated laser facets.

pattern, whereas in the 300 nm feature case, about ½ of the grating orders have a valid result. This means, the fill factor can be adjusted to ensure the design has a valid coupling coefficient.

To expand the utility of our model, the calculations for coupling coefficient, effective reflectivity, and spectral linewidth are performed for feature sizes larger than 300 nm, but with a fixed grating tooth height of 1 μm and are displayed in Figures 14, 15, and 16, respectively. In these figures, the regions where the standing wave pattern is not supported for 1550 nm emission are particularly evident. Figure 14 indicates that low order, near 50% fill factor gratings have the highest coupling coefficients, while Figure 15 show these designs also have the highest effective reflectivity. Note that in Figure 15a) for uncoated facets, most of the designs are dominated by the Fabry-Perot modes. Figure 16 indicates the low-order, near 50% fill factor gratings can provide the most linewidth reduction, and Figure 16b) clearly shows it is highly beneficial for a DFB laser to use facet coatings.

In summary, an analysis has been presented which shows that high-order DFB gratings should enable reduction of emission linewidth. If this occurs without excessive optical loss, brightness is enhanced. Figures 14-16 can be used as a guide to select design parameters of interest

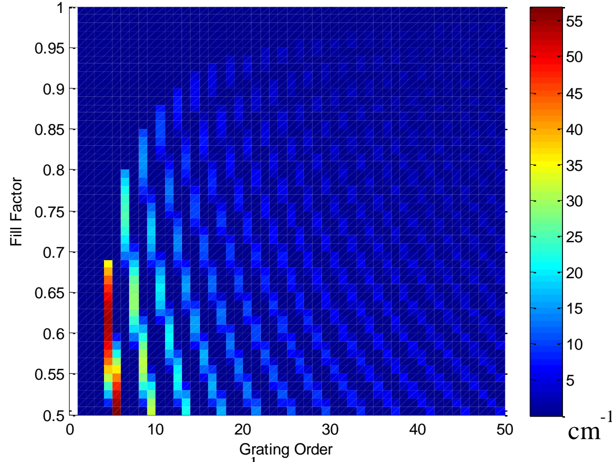

Figure 14: Coupling coefficient (color scale in cm^{-1}) as a function of grating order and fill factor for a grating tooth height of 1 μm. Unsupported grating order/fill factor combinations and feature sizes < 300 nm have a coupling coefficient set to zero.

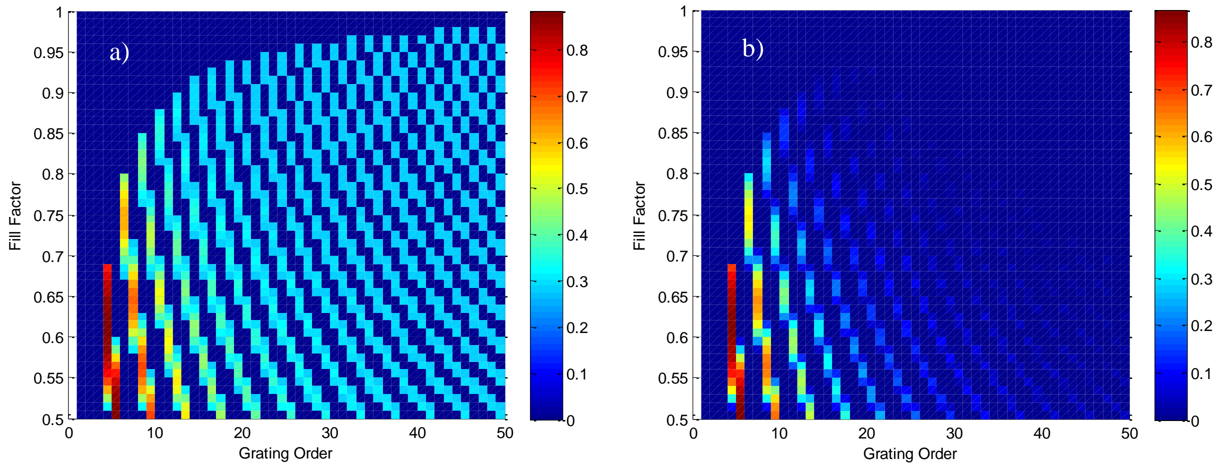

Figure 15: Effective reflectivity (color scale) as a function of grating order and fill factor for a grating tooth height of 1 μm for: a) uncoated laser facets and b) coated laser facets. Unsupported grating order/fill factor combinations and feature sizes < 300 nm are given a reflectivity of zero.

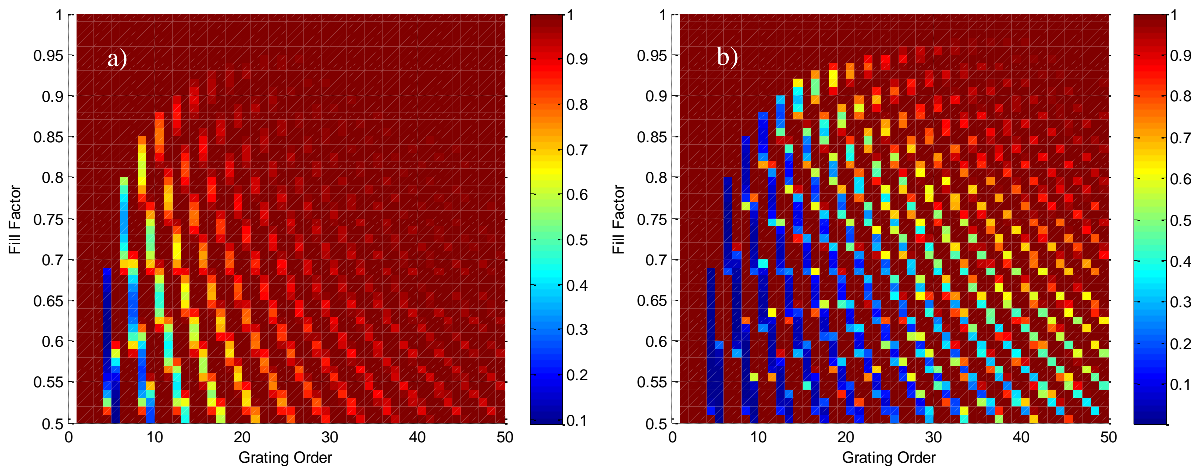

Figure 16: Normalized spectral FWHM (color scale) as a function of grating order (x) and fill factor (y) for a grating tooth height of 1 μm for a) uncoated laser facets and b) coated laser facets. Unsupported grating order/fill factor combinations and feature sizes < 300 nm are given a value of one.

for DFB laser designs. Furthermore, the model in this work can be used for optimizing specific grating design parameters like fill factor, grating order, and (in conjunction with Figure 10) feature size.

CHAPTER 4: FABRICATION

A major component of this thesis is the design and fabrication of 15xx nm semiconductor lasers based on InGaAsP materials grown on InP substrates. After a discussion of broad-area laser diodes, the fabrication process is presented in detail for both surface grating and buried grating lasers in subsequent sections. The optical lithographic mask for definition of the surface grating and the buried grating is also described.

4.1 Broad-Area Edge-Emitting Semiconductor Lasers

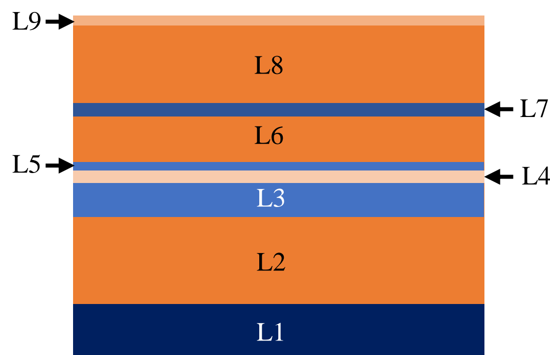

Figure 17: Laser diode epitaxial layers as described in Table 2.

The generic laser epitaxy design for a broad-area edge-emitting laser consists of a (relatively) high refractive index core region, sandwiched between two lower refractive index cladding layers to create a planar (two-dimensional) waveguide. The epitaxial layers of the laser wafers used in this research are described in Table 2 and pictorially represented in Figure 17. The epitaxial design and the wafers utilized in this dissertation were provided by Freedom Photonics, LLC. The fabricated laser diode structure is shown in Figure 18. Within the core region are one to several InGaAsP quantum wells to provide carrier confinement and serve as the gain medium. The uppermost cladding layer has p-type electrical impurities introduced while the lower cladding has

n-type impurities to create an electronic p-n junction in the waveguide. To laterally define the laser cavity within the planar one-dimensional waveguide, index-guiding or gain-guiding methods can be used. One way to create lateral index guiding is by etching a ridge on the surface of the epitaxy. Gain-guiding can be achieved using ion implantation to disrupt the crystalline lattice,

Table 2: Laser Epitaxial Structure

Layer	Description	Material	Thickness (μm)	Dopant & Type
L9	Contact Layer	$InGa_{0.47}As$	0.1	Zn, p-type
L8	Upper Cladding	InP	1.23	Zn, p-type
L7	Mode Control Layer	$In_{1-x}Ga_xAs_yP_{1-y}$	0.025	Zn, p-type
L6	Upper Cladding	InP	0.3	Zn, p-type
L5	Waveguide Core	$In_{1-x}Ga_xAs_yP_{1-y}$	0.1	Zn, p-type
L4	Quantum Wells/Barriers Active Region	$In_{1-x}Ga_xAs_yP_{1-y}$	0.044	intrinsic
L3	Waveguide Core	$In_{1-x}Ga_xAs_yP_{1-y}$	0.5	Si, n-type
L2	Lower Cladding	InP	1.2	Si, n-type
L1	Substrate	InP		n

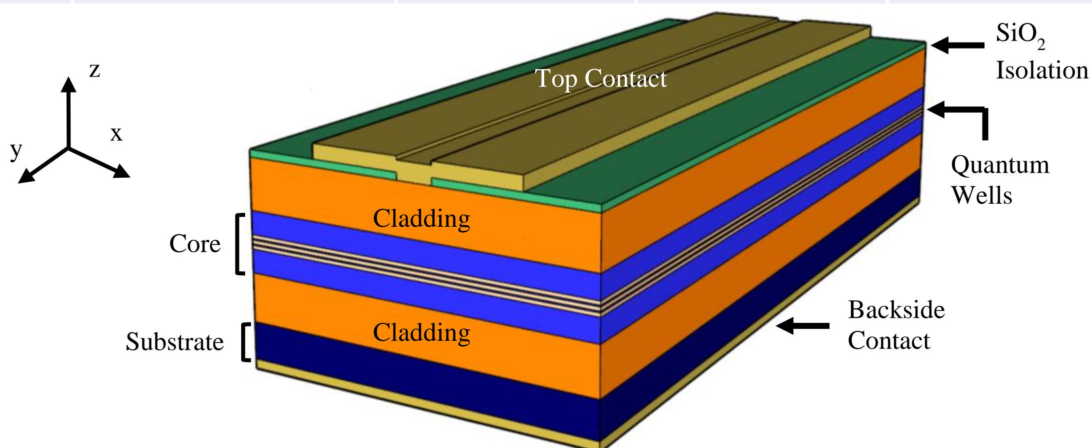

Figure 18: Illustration of a single edge-emitting laser diode. The different layers of the laser design (not to scale) are denoted. A layer of SiO_2 is used to electrically isolate each laser and for localized current injection.

compensating the impurity carriers and thus increasing resistance to restrict the carriers to flow into region which defines the laser cavity. Note that ion-implantation does not inherently change

the refractive index. However, confining the current leads to localized parasitic ohmic heating which increases the refractive index albeit indirectly. For most broad-area lasers, index-confinement is not used, but ion-implantation provides reduced carrier leakage and thus higher efficiency. However, if current spread and leakage are not issues, an alternative approach is localized injection through dielectric windows to define the gain area of the laser.

The final step in fabricating the edge-emitting laser is to cleave the mirror facets establishing the length of the laser cavity. This can be done with a scribe-and-break mechanical tool, with parameters such as strike pressure and scribe force calibrated for the sample material and thickness. The facet cleaving step must be considered from the very beginning of fabrication since the laser epitaxy will preferentially cleave along specific crystal directions. The lithography step that determines the orientation of the laser bars should be aligned at a right angle to a preferred crystalline plane to ensure clean cut laser facets. Even slight angular misalignment between the fabricated laser waveguide and the facet reduces the laser performance and may unintentionally cause the cavity to prefer certain laser modes. The mirror cleaving step is critical in determining whether an edge-emitting laser will function due to the facet sensitivity and the likelihood of introducing fatal defects. A laser device without proper mirrors or sufficient mirror reflectivity cannot satisfy the feedback condition to achieve lasing. Even if the cleaved mirrors are functional, imperfections in the mirror facets can create opportunities for premature device failure. For instance, when a laser with a facet imperfection is pumped with substantial current a localized hotspot is created on the mirror surface will cause catastrophic mirror damage and destroy the device. Once the mirror facets have been created, it is possible to test the laser diodes.

4.2 Surface Grating Lasers

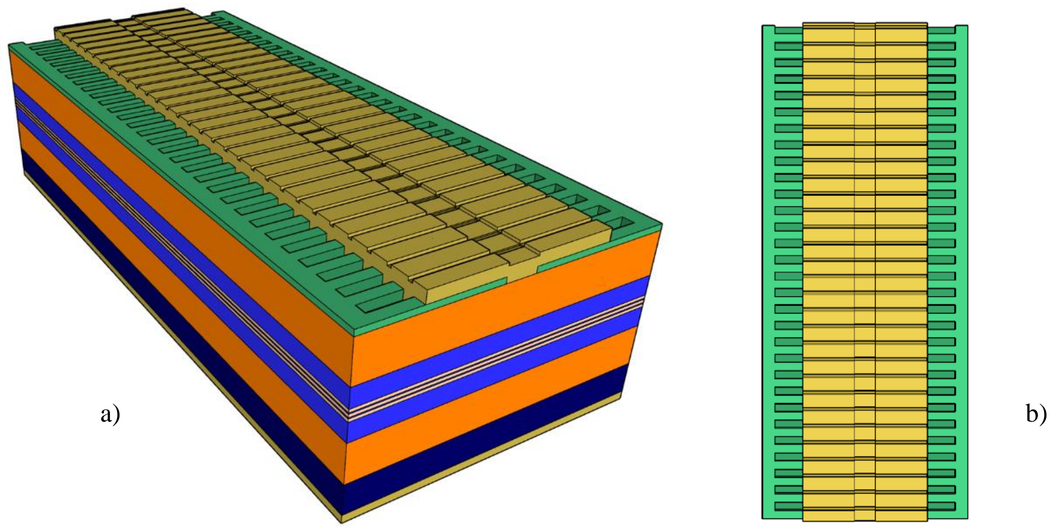

Figure 19: Illustrations of a single edge-emitting laser diode with an etched surface grating a) full view and b) top view.

Surface-etched DFB gratings are a method for reducing the number of longitudinal modes that will propagate in a diode laser. In order to achieve single/few longitudinal mode operation, a surface grating with trenches perpendicular to the light emission direction can be implemented. The objective is to reduce the spectral width of the laser output while maintaining the capability/efficiency for high power operation. The laser design, shown in Figure 19, incorporates a grating etched into the basic edge-emitting laser epitaxy. After being lithographically defined, the grating is etched, the waveguide is isolated, the contact area is defined, and then the top metal contact is deposited leaving a continuous top contact as shown in Figure 19b). Using the analysis of Chapter 3, higher-order gratings are designed that are compatible with standard contact optical lithography. To define the grating, a SiO_2 mask is patterned to withstand the plasma etching process. The optical masks designed for transferring the grating pattern are described next.

4.3 Longitudinal Grating Mask

There are three optical lithographic mask levels used in fabricating the surface grating edge-emitting lasers in this dissertation: a grating mask, waveguide definition mask, and a contact mask level. The grating mask was designed to incorporate a variety of grating orders and fill factors, with smallest dimension of 1 μm. The period length for a particular grating order is 0.48 μm times the grating order using Equation (1) and a refractive index of 3.2377. The grating mask includes gratings from 9th to 60th order. The 1 μm minimum feature size is limited by the optical mask and the achievable manual alignment accuracy of the i-line lithography systems. Small grating orders are typically preferred in the literature since the goal is often not on high power, but ultra-narrow laser linewidth.

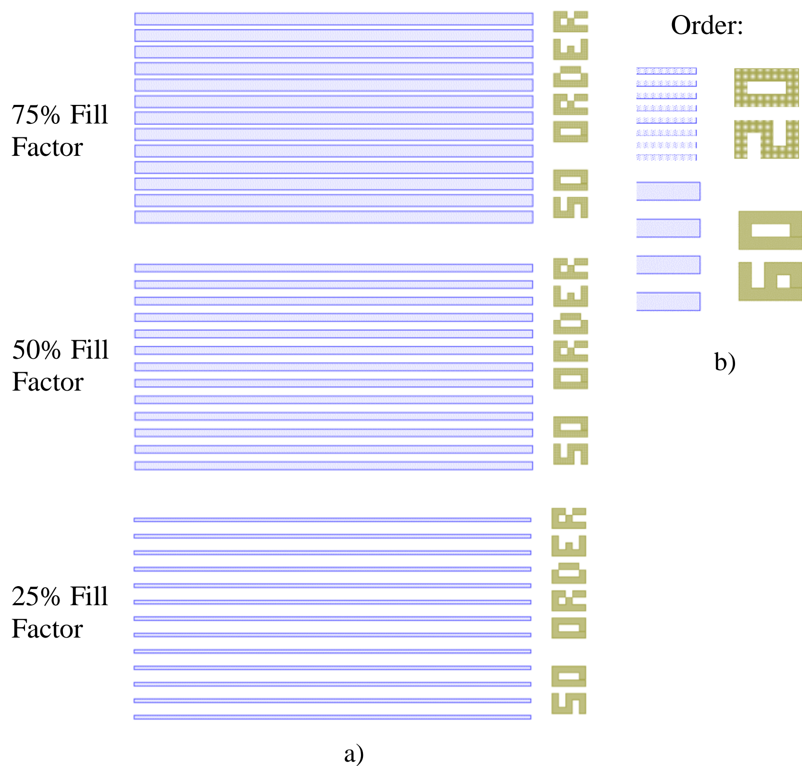

Figure 20: Grating mask pattern images. All gold text denotes the corresponding grating order. For scale, the width of the gold characters is 15 μm. On the physical mask all colored data is covered in metal. Examples of grating parameters: a) variation of fill factor and b) grating order.

A 3 x 3 inch Cr-on-quartz lithographic mask has been designed for use for both surface-etched and buried grating broad-area DFB lasers. A total of 56 different laser designs are included where the grating pitch and fill factor are varied. For an operating wavelength of 1550 nm, grating pitches that correspond to the 9th to 25th orders, and fill factors of 25%, 50% and 75% are included in the mask design. An example of the different fill factors for the 50th order case is shown in Figure 20 and the size difference between grating orders (20th and 60th) is depicted on the right. All designs for grating order higher than 25th (except the 50th order), are realized with 50% fill factors only. The grating mask was used for both positive and negative tone lithography where the negative tone lithography yielded better feature fidelity.

The waveguide definition mask is used for to periodically define a 30 μm waveguide within each device location with gaps at the ends of each device to allow for cleaving 2 mm long devices. The laser contact mask is very similar to the waveguide mask but has much wider openings so that the Au contact overlaps the un-implanted region or through the contact window. The contact mask also includes cleave guides for the separation of laser devices into die with 20 or fewer devices per die. For the buried grating lasers fabricated in this work, there is an additional mask to produce deeply etched fiducial marks so that alignment to those features will be visible after regrowth. The fiducial mask is designed such that the longitudinal grating mask and all subsequent masks can be aligned to it.

4.4 Surface-Etched Grating Distributed Feedback Laser Fabrication

For this project, surface grating DFB lasers have been fabricated using the process outlined in Figure 21 and described as follows:

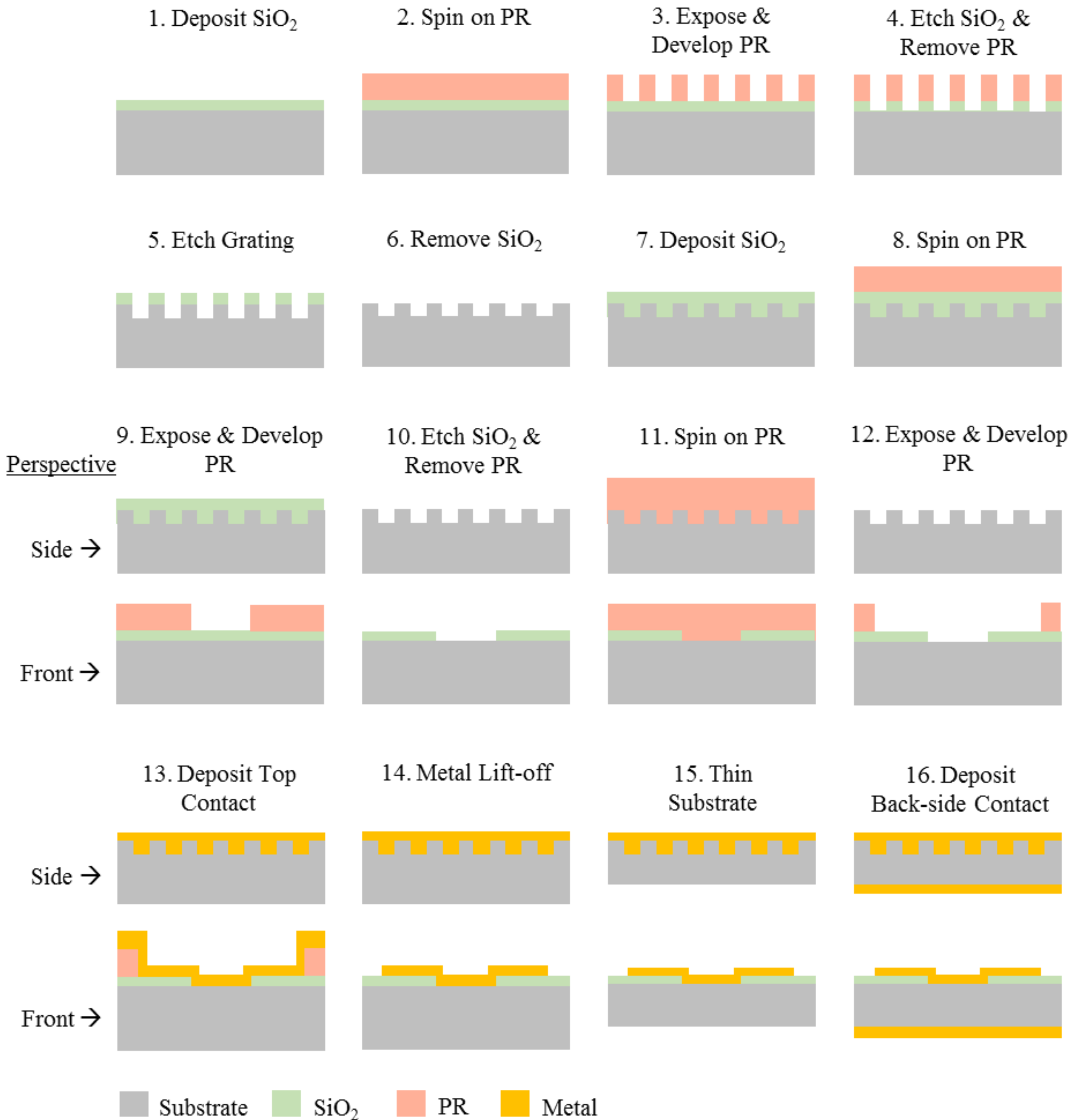

Figure 21: Diagrammatic cross-section representation of the fabrication steps for a broad-area diode laser with a metal filled surface grating. Materials are coded by color, as indicated by the key. Note steps 9 to 16 show both the side and front perspectives.

Step 1. Deposit 200 nm of SiO_2 onto the blank, cleaned, epitaxial structure with plasma-enhanced chemical vapor deposition (PECVD). This layer will form the hard mask used for the surface grating definition. The SiO_2 thickness is chosen to minimize the etch time required

to define the hard mask, thereby lessening the thickness requirement of the soft mask used for pattern transfer. A thinner soft mask will yield higher resolution features when using contact lithography. The minimum SiO_2 thickness is limited by the etch selectivity of the InP dry etch.

Step 2. Spin an even coating of photoresist (PR), in this case AZ 5214, onto the SiO_2 surface. It is critical to prime the SiO_2 surface with hexamethyldisilazane (HMDS), an adhesion promoter, applied as a heated vapor primer prior to spinning on the PR. Without HMDS, small PR defined features can lift-off and migrate on the surface or disappear during development and may not be transferred to the hard mask.

Step 3. Expose the PR through the surface grating mask using standard i-line contact lithography. Develop with AZ 917 MIF Developer. The contact made between the mask and the sample during exposure is particularly important to resolving fine grating features.

Step 4. Etch the sample using inductively coupled plasma/reactive ion etching (ICP/RIE) with CHF_3 gas to transfer the pattern from the soft mask to the hard mask. This etch will also cause the PR to harden, making removal a bit more difficult. Remove the PR using acetone and light swabbing. Use a low power O_2 etch to clean away any remaining PR residue.

Step 5. Etch the sample using an ICP/RIE recipe with Cl_2, CH_4, and Ar gas to transfer the pattern from the hard mask to the epitaxial structure. The depth of the surface grating depends on the etch time, recipe, and individual machine.

Step 6. Remove the remaining SiO_2 mask using buffered-oxide etch (BOE).

Step 7. Deposit new SiO_2 to become the basis for contact isolation between devices.

Step 8. Spin an even coating of AZ 5214 onto the SiO_2 surface.

Step 9. Expose the PR through the waveguide mask using standard i-line contact lithography and

develop the result with AZ 917 MIF Developer.

Step 10. Etch the sample using ICP/RIE with CHF_3 gas to transfer the pattern from the soft mask to the hard mask. Remove the PR by degreasing the sample and use a low power O_2 etch to ensure a clean contact surface.

Step 11. Spin lift-off resist LOR 30B and AZ 5214 PR onto the sample with sufficient thickness for metal lift-off.

Step 12. Expose the PR through the contact mask using standard i-line contact lithography and develop the pattern with AZ 917 MIF Developer.

Step 13. Deposit the top contact using e-beam evaporation of Ti (20 nm) and Au (1 μm). The thick metal is used to fill in the surface grating to create a single contact for current distribution across the device.

Step 14. Lift-off the excess metal using PG Remover to dissolve the PR layer.

Step 15. Mechanically thin the substrate using lapping techniques.

Step 16. Deposit the back-side contact with e-beam evaporation and anneal the contacts.

Step 17. Cleave laser facets with scribe-and-break tool (not shown in Figure 21).

A detailed instruction sheet for the surface-etched grating laser fabrication process using the equipment at the Holonyak Micro & Nanotechnology Lab is included in the Appendix.

Surface-etched DFB lasers have been fabricated and some example designs of the surface grating lasers are shown in Figure 22. Note in Figure 22a) the slightly indentation in the center of the gratings delineates the 30 μm waveguide width. The grating design is present underneath the waveguide and extends beyond the metal boundary. Figure 22a) and 22b) are images of a 14th order grating with 50% fill factor. In Figure 22b), the cross-sectional image shows the epitaxy covered by the SiO_2 insulation layer at the edge of the sample followed by the ridgeline of the gold

contact. Figure 22c) is the image of a 50th order grating with a 25% fill factor, where the slight indent in the center of the image is waveguide. Finally, Figure 22d) is a microscope image of the devices before cleaving. The break in the gold waveguide stripes is used as a cleaving alignment guide, and to facilitate the metal lift-off process.

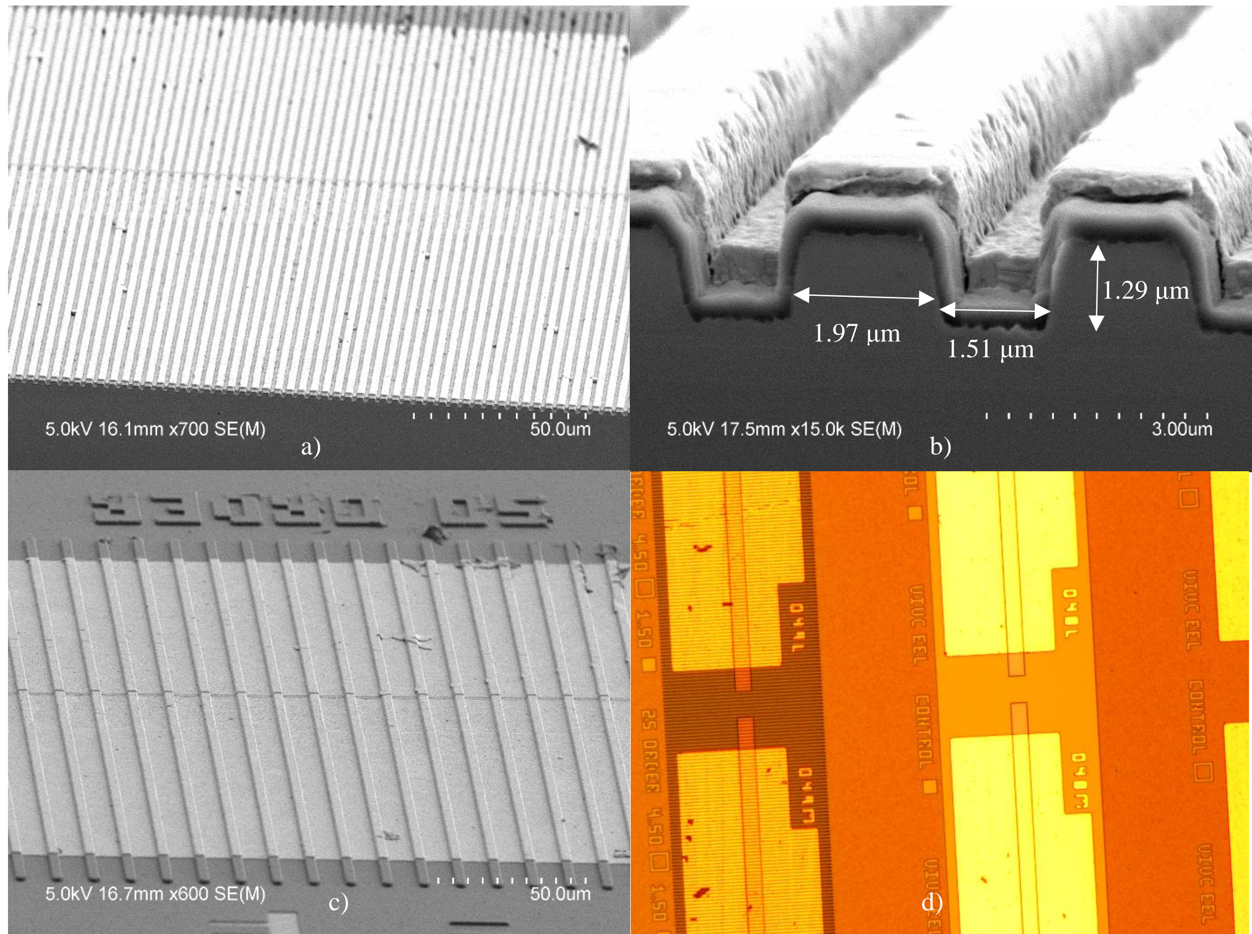

Figure 22: Images of surface-etched DFB lasers: a) 14th order grating laser cross-section, b) magnified 14th order grating with expected 1.68 µm trench and tooth width, c) 50th order grating laser with 25% fill factor with expected 3 µm tooth and 9 µm trench width, and d) optical image of uncleaved laser cavities.

As will be discussed in Chapter 5, the performance of the surface-etched DFB lasers was poor, and few DFB lasers were observed, although the control lasers (without grating) were found to be viable. Notice in the close-up cross-section image in Figure 22a) the quantum wells nor

waveguide core are apparent. From Table 1 the waveguide core is located 1.655 µm from the wafer surface, as compared to the 1.29 µm etch depth.

4.5 MOCVD Buried Grating Distributed Feedback Laser Fabrication

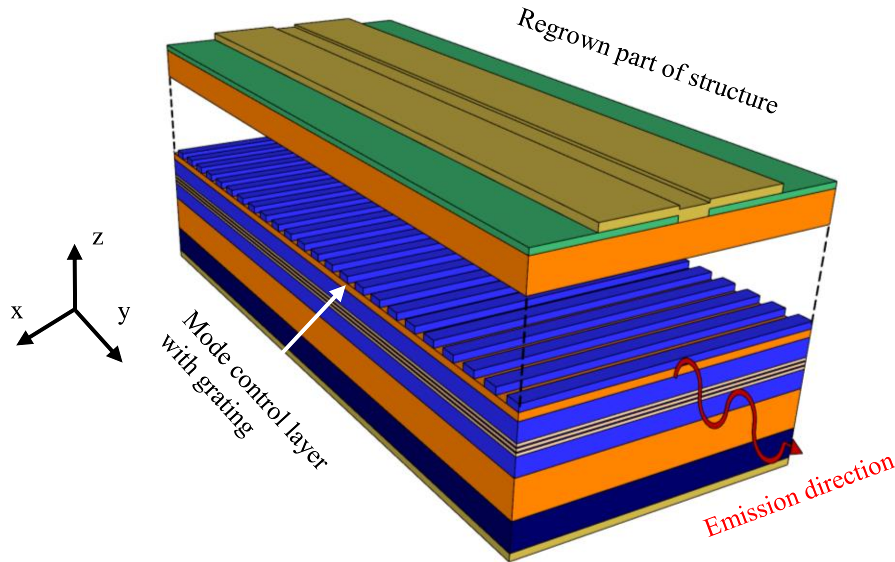

Figure 23: Buried grating DFB laser. The mode control layer within upper waveguide contains the grating. The dotted lines indicate the break between the regrown epitaxy and the etched grating.

Buried grating DFB lasers were also subsequently fabricated using the same lithography masks and epitaxial design. A sketch of a DFB laser with a buried grating in the mode control layer located within the top waveguide cladding, is displayed in Figure 23. The fabrication of buried grating lasers is significantly different, since this laser structure requires epitaxial overgrowth on the etched grating surface. Thus, an additional mask is used to introduce fiducial marks that can be seen after regrowth is complete. Wet etching was used to transfer the grating pattern into the mode control layer shown in Figure 23. Immediately before the regrowth step, an addition chemical cleaning step is performed. Figure 23 illustrates the top waveguide cladding and contact layer that are epitaxially overgrown.

The epitaxial regrowth was performed by metal-organic chemical vapor deposition (MOCVD) within the Holonyak Micro and Nanotechnology Laboratory cleanroom at the University of Illinois, in Urbana, IL. The MOCVD operation, regrowth, and material growth recipe was contributed to this project by Dr. Jeongho Park. For the buried grating, the starting epitaxial wafer is grown up to mode control layer, L7, in Table 2. After the grating is defined and etched, layers L8 and L9 and an InP cap layer are deposited by MOCVD. The buried grating laser fabrication process is pictured in Figure 23 as described next (individual steps of lithography are omitted):

Step 1. Perform fiducial mark soft mask lithography with AZ5214.

Step 2. Wet etch through the InP cap with diluted HCl and through the mode control layer with diluted nitric acid. Follow with another HCl wet etch to partially etch through upper cladding of the waveguide in the epitaxial direction (L6). Remove the remaining PR.

Step 3. Perform grating lithography with AZ5214 PR and HMDS.

Step 4. Wet etch through the InP cap and mode control layer with diluted HCl and nitric acid, respectively. Remove the remaining PR.

Step 5. Degrease extensively and manually swab. Clean the sample with a 1000 W O_2 etch to remove debris followed by a cleaning etch in BOE to remove any native oxide. Immediately load into MOCVD reactor and grow the rest of the laser structure.

Step 6. Deposit SiO_2 to become the basis for contact isolation between devices.

Step 7. Perform waveguide definition lithography with AZ5214.

Step 8. Etch SiO_2 using ICP/RIE with CHF_3 gas. Perform conductivity testing to ensure loss is not introduced by residual SiO_2 within the waveguide.

Step 9. Perform top contact lithography with AZ5214 and LOR.

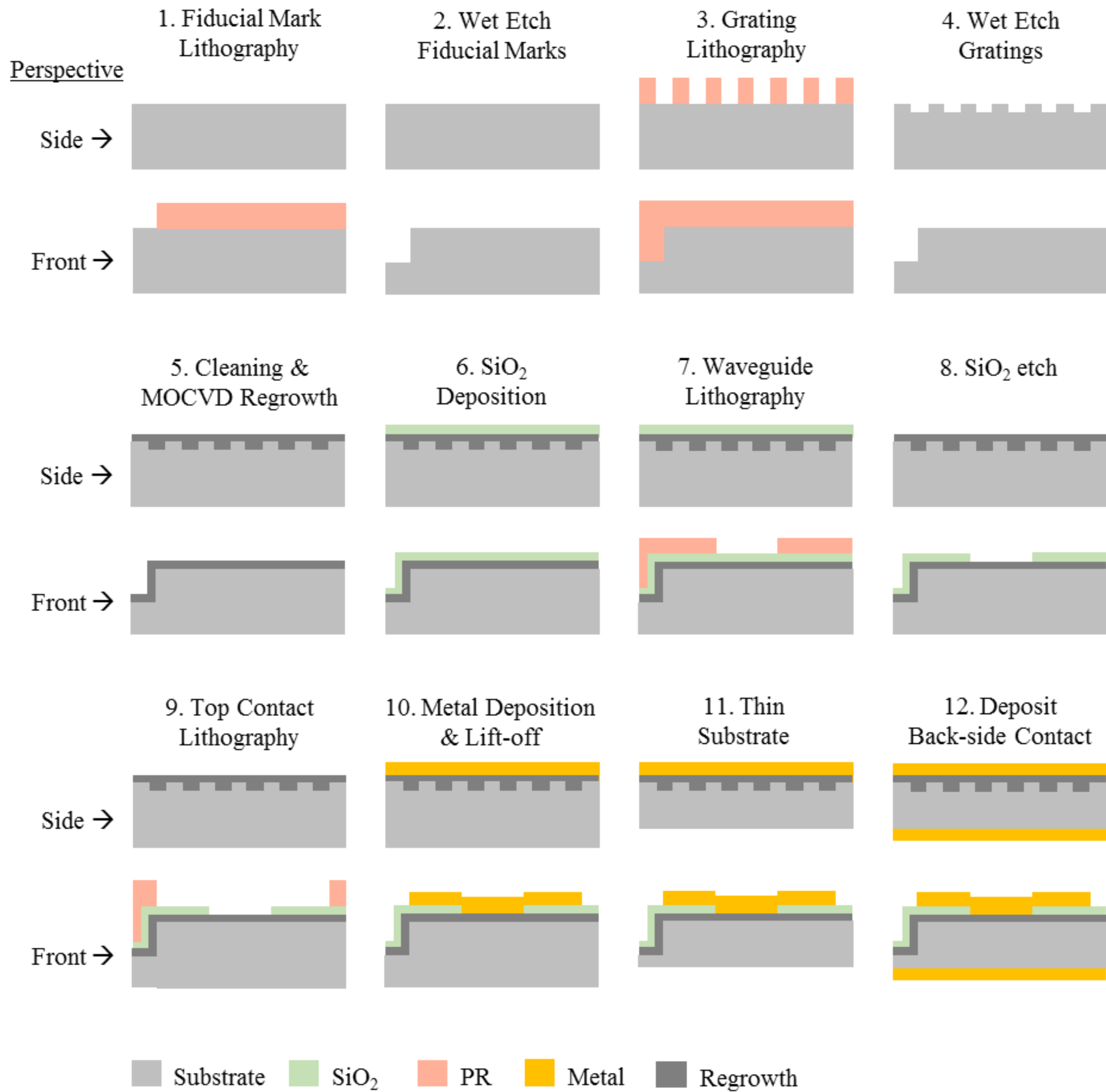

Figure 24: Diagrammatic cross-section representation of the fabrication steps for a broad-area diode laser with gratings buried by MOCVD regrowth. Materials are coded by color, as indicated by the key. All steps are shown from the front perspective and side perspective as if cut through the device center.

Step 10. Deposit the top contact using e-beam evaporation of Ti and Au. Perform metal lift-off with PG Remover.

Step 11. Mechanically thin the substrate using lapping techniques.

Step 12. Deposit the back-side contact with e-beam evaporation and anneal the contacts.

Step 13. Cleave laser facets with scribe-and-break tool (not shown in Figure 23).

A fully detailed worksheet for the buried grating laser fabrication process is included in the Appendix.

Optical images of the fabricated devices are shown in Figure 25. The MOCVD regrowth appears to planarize the surface, thus the gratings are not readily apparent after regrowth. Figure 25a), 25b), and 25c) were taken before regrowth for 50% fill factor gratings of order 45, 19, and 16, respectively. Figure 25c) is an excellent example of lift-off of the grating high index layer, which occurred due to delamination during the wet etch step, and created feature drift. For the devices produced for this thesis, only those with feature sizes below 2 μm exhibited this flaw. The

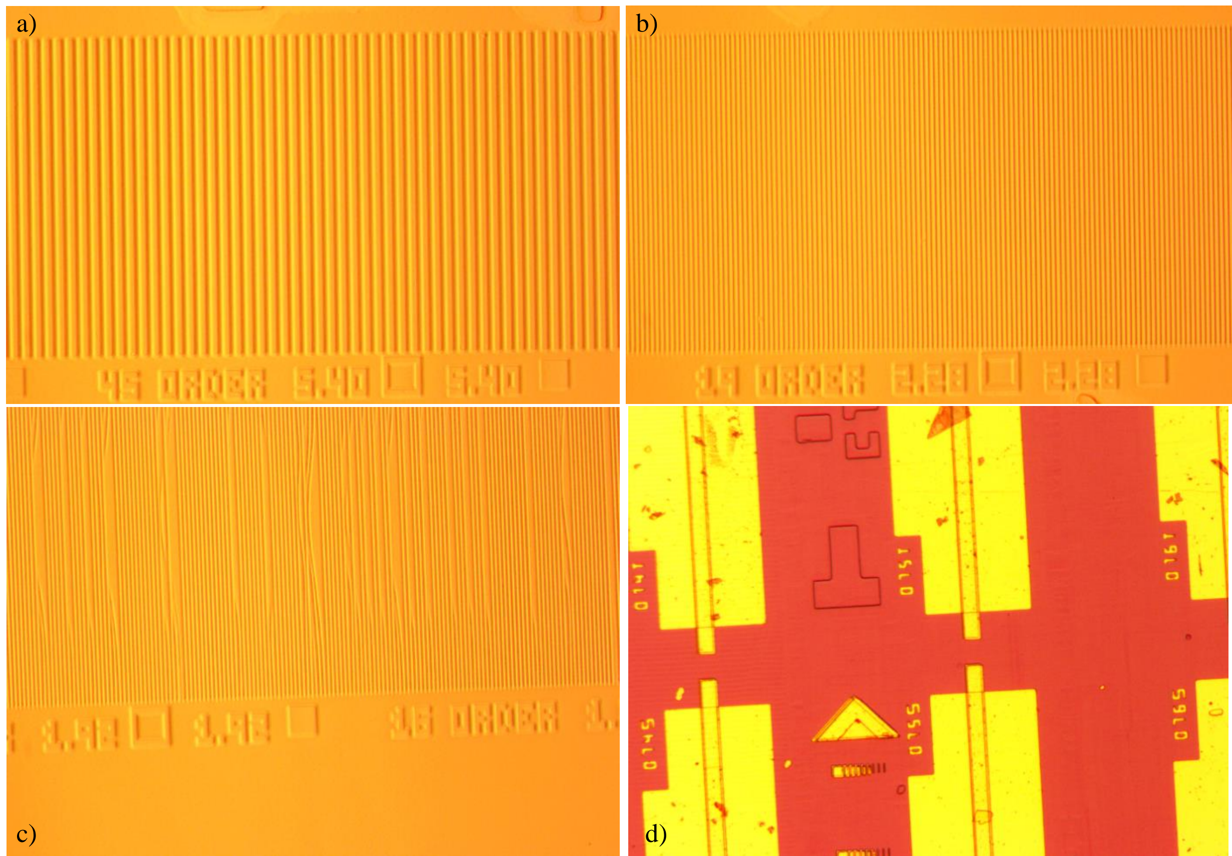

Figure 25: Edge-emitting lasers with buried DFB gratings during fabrication: a) 45th order grating with 50% fill factor with 5.4 μm feature sizes prior to regrowth, b) 19th order grating with 50% fill factor with 2.28 μm feature sizes prior to regrowth, c) 16th order grating with 50% fill factor with 1.98 μm feature sizes prior to regrowth, and d) optical image of uncleaved laser cavities.

problem can be remedied by using dry etch grating definition. In Figure 25d) the uncleaved buried grating lasers are shown, and do not show the obvious grating pattern as seen in Figure 22d).

4.6 Laser Facet Coating

The final steps of edge-emitting laser fabrication are facet cleaving and optional (but recommended for high power lasers) facet coating, to increase one facet to near perfect reflectivity with a HR coating and decrease the other facet to a reflectivity on the order of 0.01 with an AR coating. This allows the laser to emit preferably in one direction and can dramatically enhance the power output at the AR facet. Finally, as shown in Chapter 3 and as evident in the comparisons shown in Figures 9, 13, and 16, HR/AR facet coating can dramatically influence the efficiency of high-order gratings and enable viable grating designs that produce linewidth reduction.

Laser coating was purposely avoided in all iterations of DFB laser fabrication in this project. Since this is the first high power laser research in this group, we avoided coatings to minimize laser safety concerns and coating compositions are proprietary information (and additional cost). As shown in the theoretical results in Chapter 3, it would be highly beneficial in the future to coat the laser diodes, since the degree of effective DFB reflectivity changes dramatically with a coating. Furthermore, commercially manufactured laser diodes are always coated so experimental consistency makes results more relevant to the state-of-the-art. Lastly, CW lasing operation is more easily achievable with coated facets.

4.7 Alternatives to I-Line Lithography

An overarching motivation for this research is to apply high-volume manufacturing techniques for broad-area DFB laser production. Two alternatives to e-beam lithography for

grating definition that were introduced in Chapter 2, VUV microplasma lithography [42] and direct UV laser lithography [13], will be outlined in this section for producing gratings with smaller feature sizes than those in the DFB lasers fabricated in this thesis. Lithography techniques that rely on light for pattern transfer are inherently limited by the wavelength of the light used. Diffraction, the bending of light as it goes through an aperture, is a wavelength dependent resolution limitation and improves using shorter wavelength emission for patterning. Therefore, smaller feature definition is expected using a VUV microplasma emission source [42], such as pictured in Figure 26, with a wavelength of 172 nm for contact lithography. Common photoresists designed for i-line lithography (e.g. AZ 5214) do not undergo sufficient photochemical change at 172 nm. We have experimentally confirmed that an electron-beam resist, PMMA, can be patterned at this wavelength as seen from the scanning electron microscope image in Figure 27. The required PMMA thickness for the etched grating depends on additional processing parameters, such as whether the resist thickness can survive a RIE step as a mask.

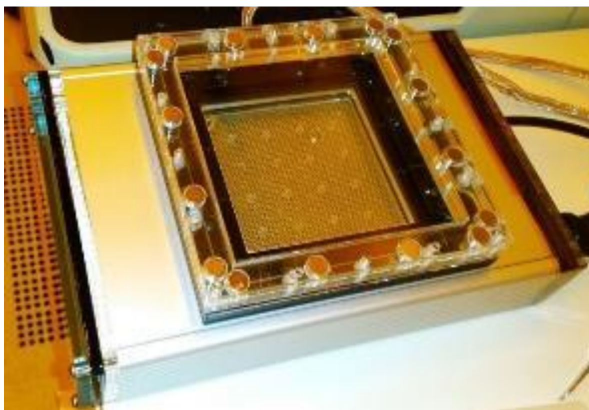

Figure 26: Image of the VUV lamp discussed in this project. The lamp exposure area is approximately 3 x 3”.

The VUV emission source requires a suitable mask to project the necessary pattern onto the PMMA. An important consideration is the material of the mask substrate, since not all materials are sufficiently transparent at 172 nm. A quartz mask has been found to have sufficient transmission for the VUV light source (unlike a soda-lime glass mask). For this project, an external

source manufactured the mask plates. Due to limitations of the commercial source for producing lithographic masks, our results to date are limited by the minimum feature size (0.8 µm) of the mask. Due to the smaller feature sizes desired, ensuring uniform contact between the mask and the sample during exposure has proved critical to achieving high feature resolution. Feature "blurring" from incomplete contact, such as that cause by stray resist or dust particles, will cause dramatic loss of resolution, more so than standard lithography.

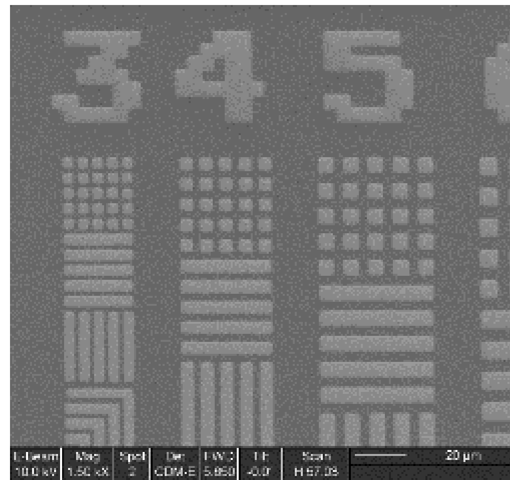

Figure 27: SEM image of PMMA features defined by VUV contact lithography. The lithographically defined numbers in the image correspond to the width in microns of the dot and line features directly below each respective value.

Another alternative is direct UV laser writing lithography, which is available within the Holonyak Micro and Nanotechnology Laboratory cleanroom. Direct laser writing uses a larger beam size than e-beam and is not capable of the same ultimate resolution, but sub-micron feature resolution is possible using a system that is less expensive to purchase and maintain. Prototype gratings with approximately 300 nm grating teeth and 1 µm pitch have been defined and etched [41]. As shown in Chapter 3, the design of high-order DFB gratings that are capable of reduced linewidth, can be viewed from the perspective of the smallest feature size that can be achieved. For this reason, a 300 nm feature size is proposed for the grating designs shown in Figure 13 in Chapter 3. Similar to e-beam lithography, direct laser writing is still a serial

manufacturing process. However, since the equipment cost is much lower, this fabrication approach is excellent for research and development prototypes, while multiple laser writing systems in parallel has the potential to meet the needs of small-scale manufacturing.

CHAPTER 5: LASER DIODE CHARACTERIZATION

The 15xx nm laser diodes fabricated in this project, as described in Chapter 4, using the designs discussed in Chapter 3, are experimentally characterized in this chapter. After a discussion of the laser testing protocol, the characteristics of surface-etched and buried grating DFB lasers are presented.

5.1 Testing Considerations

When testing unpackaged edge-emitting laser diodes, there are several considerations that must be taken into account: the die size for handling, type of cooling, current injection method, and current source operating parameters. Packaging laser diodes alleviates several of these concerns by eliminating the need to manually handle the die and robustly incorporates heat sinking, wire bonding, and the potential for adding active cooling. However, packaging was not pursued for the lasers fabricated and studied in the dissertation. The laser cavity length was chosen to be 2 mm to allow for relatively straightforward die handling. Passive heat sinking with a gold-plated copper chuck is used during the testing conducted in this thesis.

Another consideration is ensuring uniform current injection along the approximately 2 mm laser cavity. This is necessary to prevent localized injection “hot spots” that might occur along the cavity, that might be exacerbated due to the surface-etched grating. A custom designed wedge-style multi-tipped (~20 connected in parallel along 1.8 mm length) electrical probe was used for laser testing. Unfortunately, the multiple tips do not make electrical contact well with lasers having narrow (30 μm) top contacts, so the top contact width was changed in later fabrication iterations to > 100 μm. The important addition of an independent probe tip to the wedge was made to

accommodate accurate voltage sensing (with at least one or more independent sensing tips recommended for future probes to ensure redundancy).

The laser diodes were characterized at the die level under quasi-CW pulsed operation. Continuous wave lasing operation from probed die was not observed using the experimental setup. A quasi-CW current source was used to drive the lasers at 100 Hz with a 0.5% duty cycle with approximate pulse width of 100 μs. The pulsed output power and emission spectrum were measured. With pulsed operation there are thermal effects that influence the laser performance that become greater with longer pulse width. One effect is the thermal spectral shift induced in the laser emission during the operation over a current pulse: as the laser increases temperature the increasing refractive index causes an addition spectral shift. Because of this effect, the measured spectra in this report are always measured to be wider than they actually are, but all measurements are taken under the same conditions, so relative comparisons can be made. This allows comparisons of the DFB lasers with control (no grating) lasers fabricated in the same die and characterized at the same time. The thermal broadening can be exacerbated by the data acquisition time, so the peak hold function on the optical spectrum analyzer (OSA) should be adjusted. The spectra can be captured more accurately by using a faster pulsing current source.

5.2 Laser Diode Characterization Setup

The edge-emitting laser diode testing setup constructed for this research is pictured in Figure 28 and a block diagram version is reproduced in Figure 29 where the optical path and electrical connection are separately denoted. The electrical connections are displayed by black lines in Figure 29 and use either 12 AWG or a standard banana-plug wiring to prevent heat damage. The sample platen is a gold-plated copper block with a vacuum hole drilled through it. Laser die

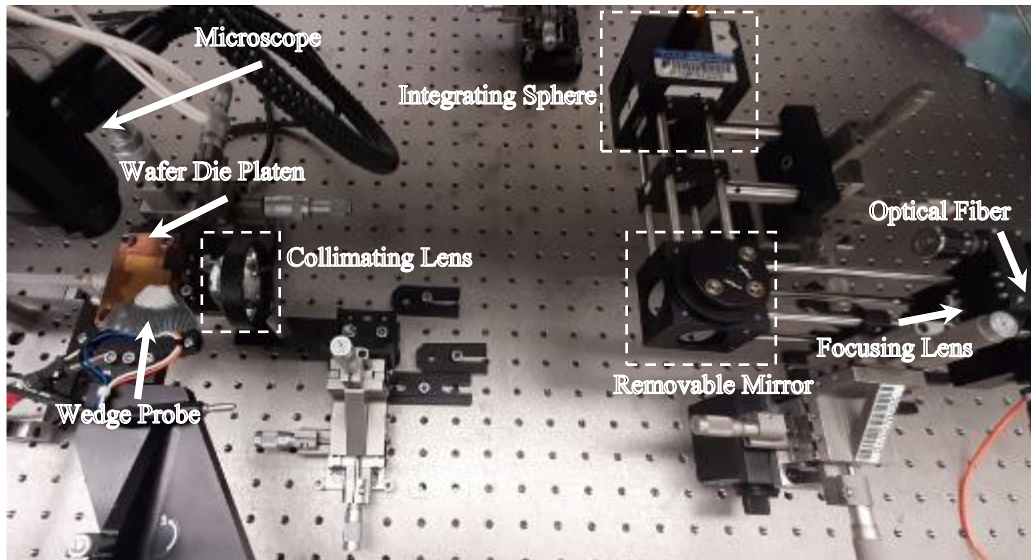

Figure 28: Picture of the edge-emitting laser diode characterization setup with parts labeled.

(approximately 1 cm x 2 mm) are secured to the platen by vacuum. The current is injected into the lasers using a wedge probe connected to the quasi-CW current supply. The probe also has a lead for measuring the applied voltage. An integrating sphere paired with an internal photodetector produces a current proportional to the intensity of the received light. Both the voltage signal and photodetector current output are measured by an oscilloscope and digitally recorded by a computer through a GPIB connection. A data acquisition program was written in Python to automate the collection of current, voltage, and emission intensity of the pulsed laser operation. All computer interfacing, instrument communication, and Python coding was contributed by Pawel Strzebonski.

The optical path of the laser emission to the OSA or the integrating sphere is pictured in red in Figure 29. The laser die are handled with vacuum tweezers and positioned fairly reproducibly on the platen with the aid of a custom designed insulating backstop to eliminate angular variation in placement and minimize the die sliding from probe movement. There is still slight angular variation between each die placement, which is accommodated in the system design by ensuring the components are capable of angular adjustment on a single axis as well as in three dimensions. For spectral measurements, the laser emission is focused into an optical fiber and

reaches the OSA. For power measurements, a removable mirror is inserted after the light is collimated to redirect the light into the integrating sphere. Measurements were gathered by adding/removing the mirror for each successive laser diode.

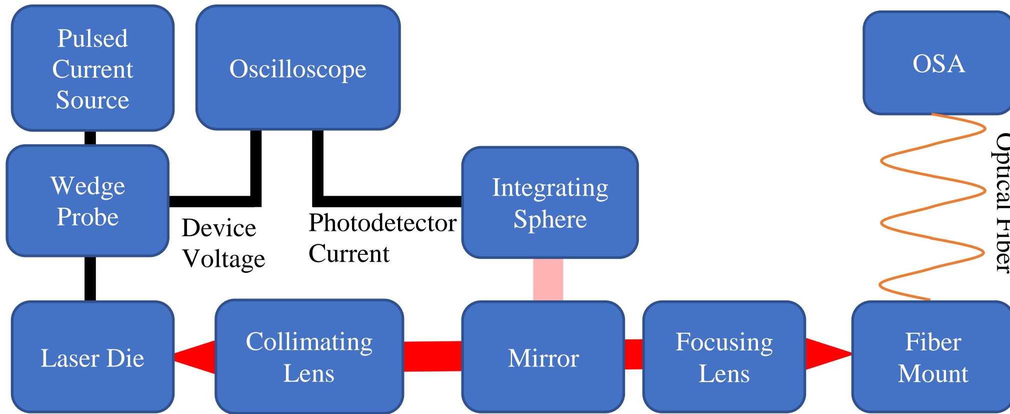

Figure 29: Block diagram of edge-emitting laser diode characterization setup showing the electrical path and the optical path. The light path to the integrating sphere is active when the mirror is in place at a 45 degree angle.

5.3 Surface-Etched Grating Distributed Feedback Laser Characterization

Two iterations of surface-etched grating DFB lasers were fabricated. For both attempts, no lasers with etched grating achieved lasing operation. Only the control (unetched) lasers on the first iteration lased. However, lessons were learned that enabled subsequent successful lasers. For example, the use of HCl was eliminated due to rapid InP etching. Facet cleaving was also determined to be a limiting factor. After the first laser fabrication iteration, all facet cleaving for the laser die was done courtesy of Freedom Photonics. The commercial laser bars manufactured by Freedom Photonics use die with the same approximate dimensions. Hence, we are able to compare tested lasers from the same die. The second iteration of surface-etched lasers also did not lase. It is likely the deep etched grating created excessive optical loss which prevented laser operation, even under pulsed conditions. Another possibility is the SiO_2 isolation layer contained

gaps caused by the ridged surface of the grating. This can be remedied by increasing the SiO_2 layer thickness in future trials.

5.4 Buried Grating Distributed Feedback Laser Characterization

Buried grating DFB lasers have been fabricated, as discussed in Chapter 4, using the same lithographic mask. As will be shown, nearly all grating designs have demonstrated lasing operation under quasi-CW injection. The laser emission spectra and output power are measured as a function of current. The output intensity is given in arbitrary units, which nevertheless allows the threshold current to be determined. Measurements of the lasing emission linewidth were made from multiple

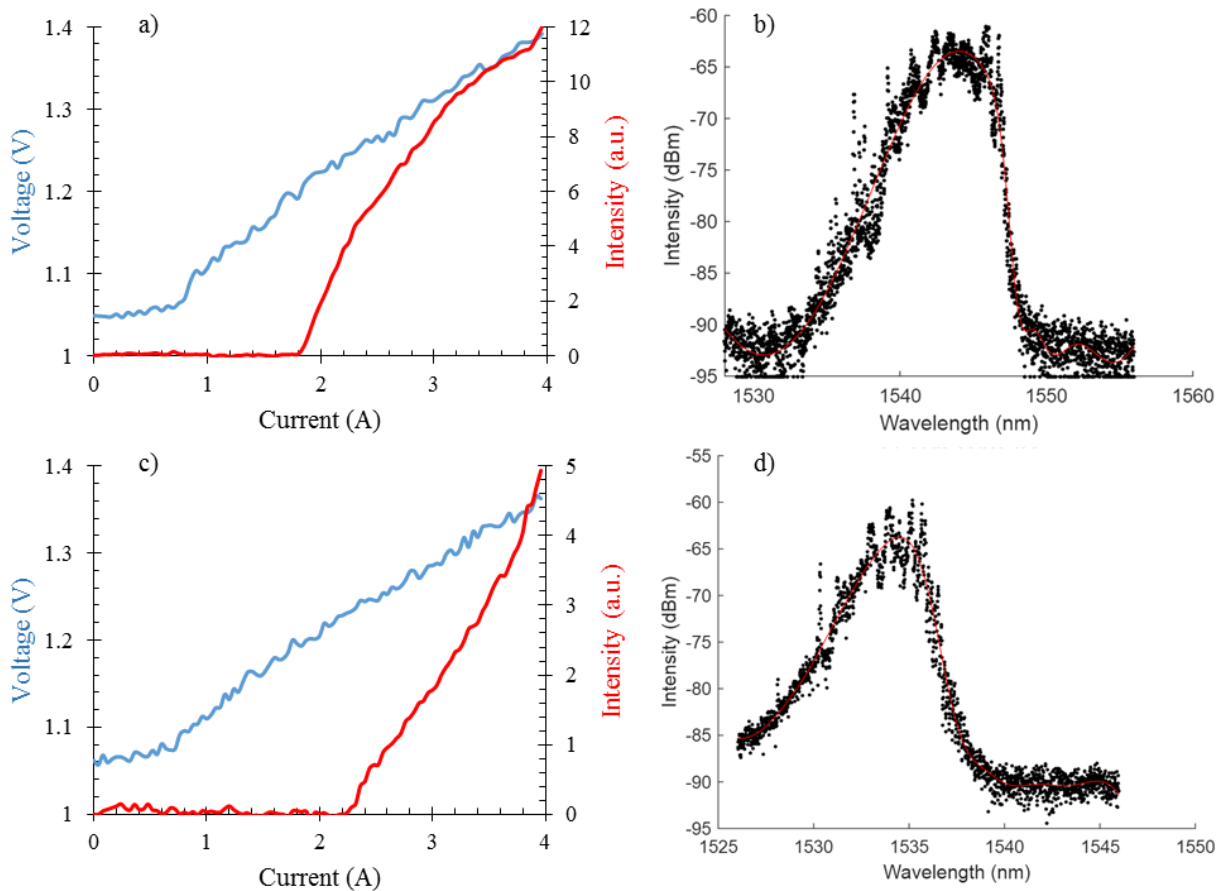

Figure 30: Examples of captured data: a) LIV of a control device, the blue curve (left axis) is the IV and the red curve is the LI (right axis), b) emission spectrum of a control device with a sum of multiple Gaussian fitting curve (red), c) LIV of an 18th order grating, 50% fill factor device, and d) emission spectrum of an 18th order grating, 50% fill factor device with a sum of multiple Gaussian fitting curve.

different laser die with the objective of characterizing at least one of each fabricated grating design. Multiple control (non-grating) lasers within the same die were also measured.

Figure 30 shows the light output versus injected current and applied voltage (LIV) and the spectral linewidth. Characteristics for a 30 µm wide control laser are shown in Figure 30a) and 30b) while Figure 30c) and 30d) show the properties of a laser with a 50% fill factor 18th order grating. The threshold current of the control laser is clearly lower than that of the grating laser. Figure 31 is a comparison of the threshold currents as a function of the grating order. On this plot, the average threshold current of the control lasers lacking a grating is 2.08 A +/- 0.19 A and are depicted as a 0th order grating (for display purposes) with the standard deviation of the control lasers shown as an error bar in Figure 31. A lower threshold is expected for the control lasers, since introducing a grating adds loss, in agreement with the results shown in Figure 31. Notice the variation of threshold for the grating lasers (standard deviation of +/- 0.2 A) is approximately within a single standard deviation to the control lasers. The fill factor of each design is shown by the marker shape and color. Unfortunately, due to the size of the fabricated sample, not all of the laser designs from the longitudinal grating mask were fabricated and could be studied. For grating designs that were made, nearly all of them achieve lasing with reasonable threshold current not exceeding 3 A. The experimental lasers also emitted less optical power than the control lasers at the same drive current.

The emission spectra of the lasers were also captured and characterized. For these experiments the spectral bandwidth requirement of the OSA is about ~20 nm for the noise floor to be visible and the selected scanning rate needs to be sufficiently slow to avoid intensity oscillations from the pulsed injection but fast enough to minimize thermal broadening. The lasing spectra were collected using the same OSA settings (peak hold set to 3 ms with High 2 scanning regime/rate).

To probe the reproducibility of these measurements Figure 32 is a comparison of spectral measurements gathered from the same laser using identical probing conditions, but tested on different days. Curve fitting of the spectra is performed to extract the full width at half maximum (FWHM) laser linewidth and peak wavelength. The measured laser spectra were fit to a sum of

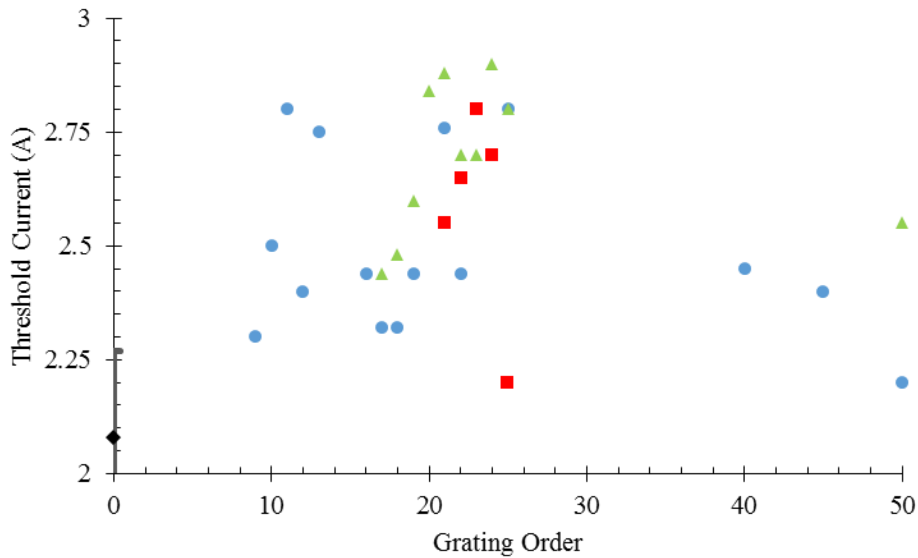

Figure 31: Experimental buried grating laser threshold vs. grating order. The fill factor is denoted by the color and shape of the markers: green triangles, blue circles, and red squares are 25%, 50%, and 75% fill factor, respectively. The black diamond point is the average of all control devices across all of the die measured with the grating order artificially set to 0 for display purposes.

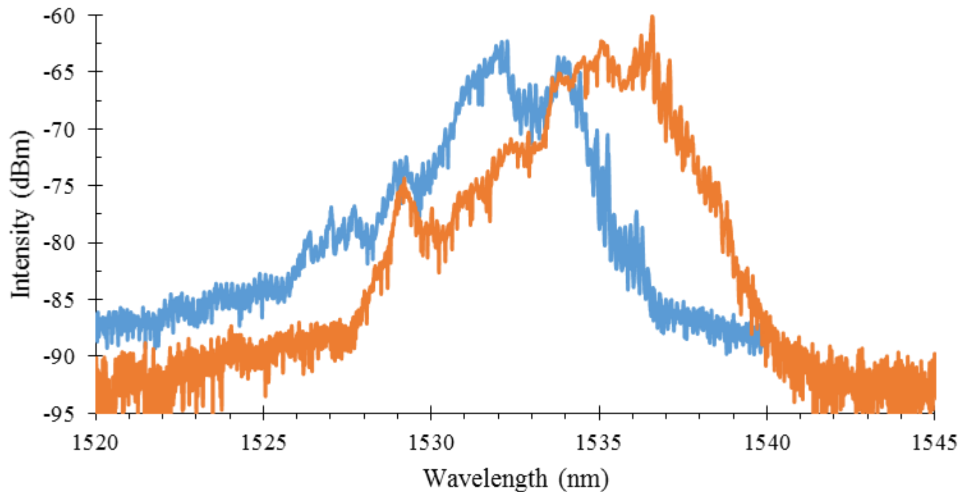

Figure 32: Comparison between two spectra gathered on different days from the same control device at the same drive current. Demonstrates the effect of heating and consistency between measurements. Gaussian fitting yields a FWHM linewidth of 3 nm for the blue curve and a peak wavelength of 1532.7 nm. The linewidth of the orange curve is 3.1 nm with a spectral peak of 1535.2 nm. Using spectral fitting assists in maintaining consistency between measurements.

Gaussian line shapes, using a MATLAB analysis. The noise floor of all spectra was set to -95 dBm. The FWHM location was then determined to occur at the fitted peak intensity corresponding to -3 dBm. The number of Gaussians (max 8) used in each fitting was decreased where necessary to make the fitting as reasonable as possible for determining the FWHM linewidth. Figure 30b) depicts a captured spectra of a control laser driven at 3 A with the curve fitting (red line)

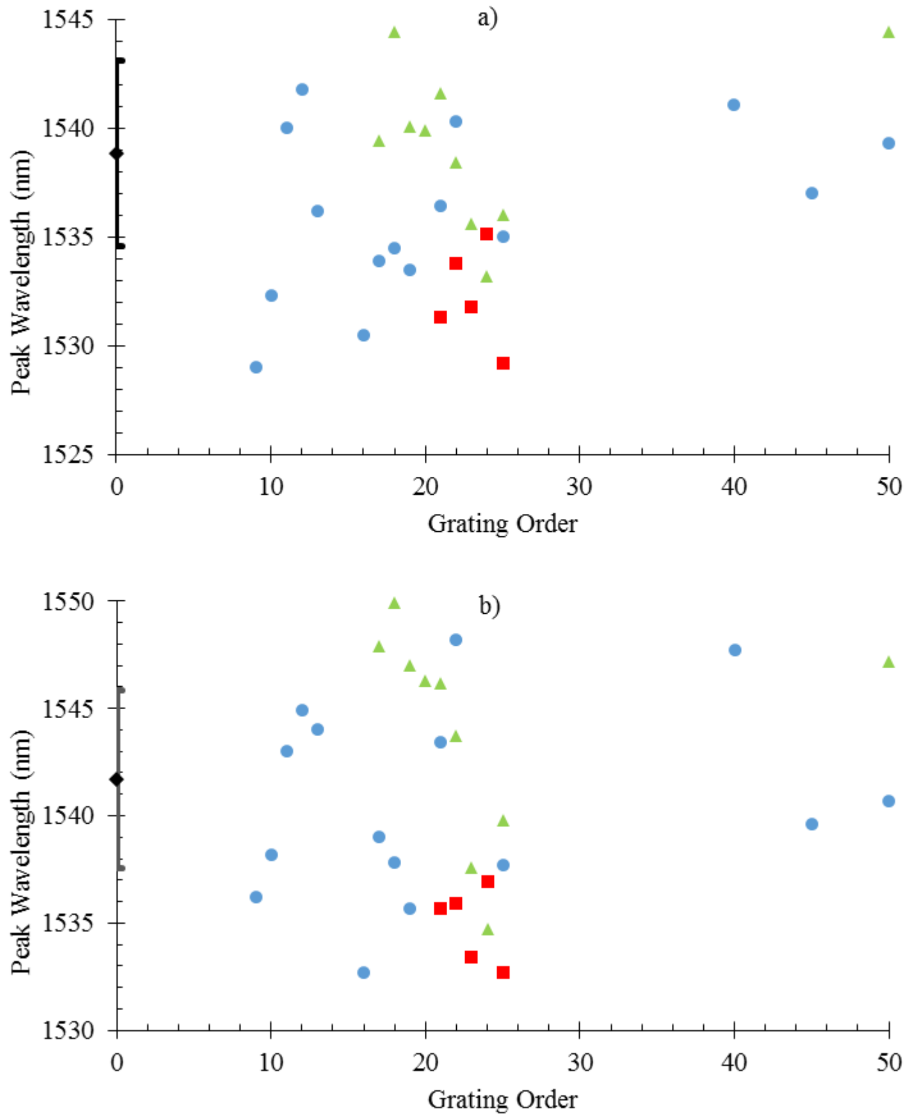

Figure 33: Experimental buried grating laser device peak wavelength vs. grating order. The fill factor is denoted by the color and shape of the markers: green triangles, blue circles, and red squares are 25%, 50%, and 75% fill factor, respectively. The black diamond point is the average of all control devices across all of the die measured with the grating order artificially set to 0 for display purposes. The lasers were driven at different currents: a) 3 Amps and b) 4 Amps.

superimposed; similarly Figure 30d) shows the fitted spectra for a buried grating laser. All lasers tested had spectra collected at a drive current of 3 and 4 A, regardless of the individual laser threshold.

The peak wavelength of each fitted laser spectrum is plotted for drive currents of 3 A in Figure 33a), and 4 A in Figure 33b). The fill factor and the averaged peak wavelength and standard deviation is denoted similarly as in Figure 31. The peak wavelength shows a trend based on the laser location on the fabricated wafer before it was diced/cleaved, rather than the experimental design parameters. The lasing wavelength is also determined by the cavity resonance, since the phase condition has to be satisfied for the exact laser cavity length. As discussed in Chapter 3, the facet cleaving process introduces some variability in cavity length and alignment of the uncoated facet with the fabricated grating. Said disparity will introduce alterations in the peak wavelength, particularly between different laser die. The grating peak wavelengths exhibit a near linear increase of lasing wavelength across each laser die. However, this trend is not considered to particularly impact the measured linewidths.

The spectral linewidth of all lasers are compared in Figure 34 for two drive currents above threshold. For this comparison, the experimental spectra are fitted as discussed above, and the FWHM of the fitted linewidth is extracted at drive currents of 3 A (Figure 34a)) and 4 A (Figure 34b)). The fill factor and the averaged control linewidth and standard deviation is denoted similarly as in Figure 31. Notice, in Figure 34a), the linewidths of many high-order grating lasers are less than the control lasers, while this is less obvious at the higher injection current in Figure 34b). The general trend is the spectral linewidth increases with grating order and approaches that of the control lasers for large grating order >30, which is consistent with the theory discussed in Chapter 3. This is particularly evident for the lasing emission above but near threshold, as apparent

in Figure 34a). At the higher drive current, more higher-order modes are expected to lase and the influence of the buried grating becomes less effective.

An example spectral comparison is made in Figure 35 between a control laser and a 16th order grating, 50% fill factor DFB laser, for which the difference in spectral width is abundantly clear. The linewidth values shown in Figure 34b) at 4 A drive current are always larger than those

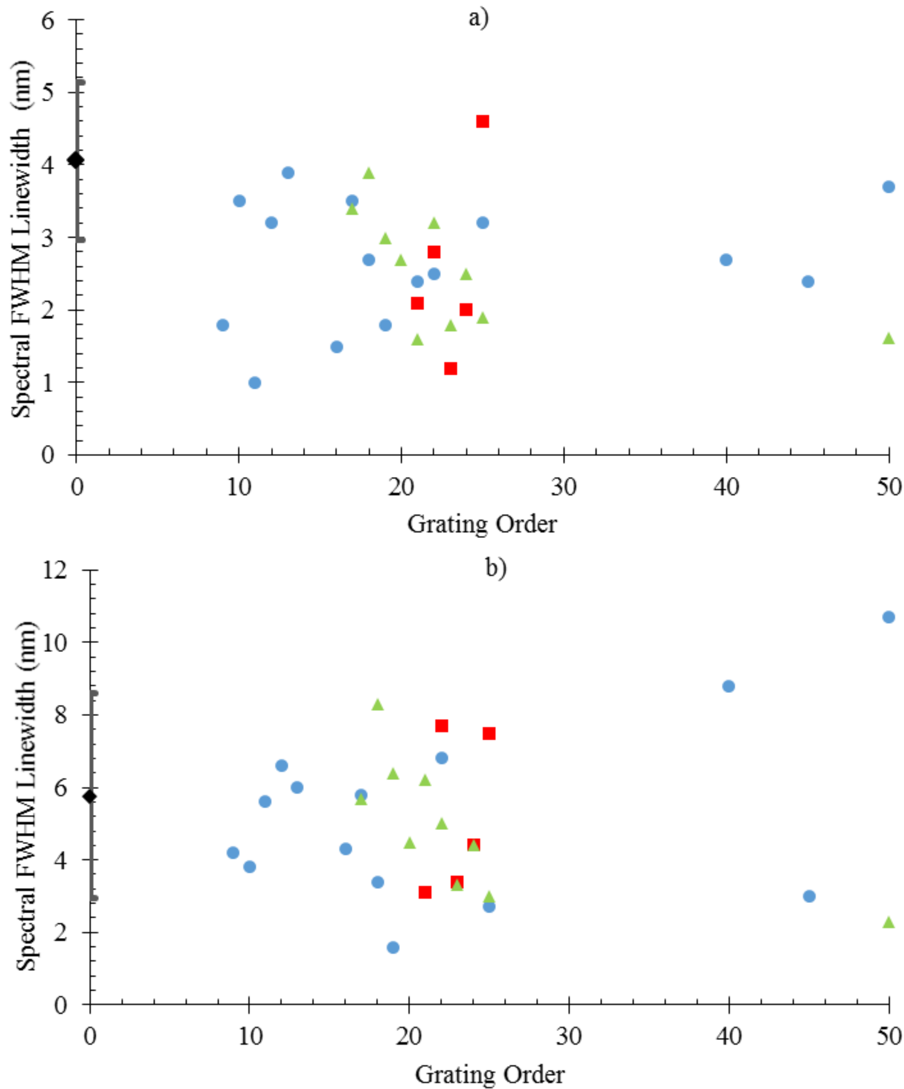

Figure 34: Experimental buried grating laser device spectral FWHM vs. grating order. The fill factor is denoted by the color and shape of the markers: green triangles, blue circles, and red squares are 25%, 50%, and 75% fill factor, respectively. The black diamond point is the average of all control devices across all of the die measured with the grating order artificially set to 0 for display purposes. The lasers were driven at different currents: a) 3 Amps and b) 4 Amps.

seen in Figure 34a) at 3 A drive current. The higher current spectra are typical of laser broadening with increased injection current and the resulting lasing of additional longitudinal modes.

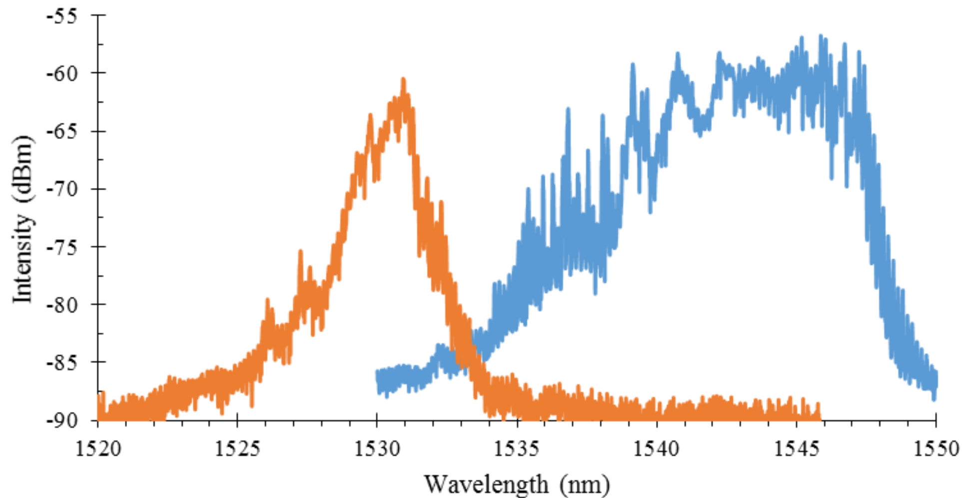

Figure 35: Comparison between two spectra from a 16th order grating device with 50% fill factor (orange) and a control device (blue). The grating structure creates a dramatically narrower spectral profile. Both lasers are driven at 3 A.

The variation in the measured emission linewidths in Figure 34 are related, in part, by the facet cleaving uncertainty. A grating is designed for a specific wavelength and this can conflict with the wavelength that satisfies the phase condition arising from the cleaved facets, generating further scattering from the grating interfaces. Using 3 A drive current, the average control lasing linewidth is 4.05 +/- 1.09 nm and that of the grating lasers is 2.60 +/- 0.88 nm. The difference between the control and grating laser linewidth average is greater than the standard deviations. Therefore, the experiment conclusively demonstrates the presence of linewidth reduction from the addition of DFB gratings into the laser structure. However, the linewidth reduction is obtained with a penalty in threshold current.

The fact that the buried grating lasers have been demonstrated as viable lasers, while the surface-etched grating devices did not achieve lasing, strongly suggests the buried gratings produce lower optical cavity loss. However, the gratings do negatively impact the lasers as evident

in the higher threshold currents observed for the grating lasers and the much lower output power at the same current as compared to the control lasers. Therefore longitudinal mode control is demonstrated using the buried high-order gratings, but this device structure requires further optimization to demonstrate an improvement in brightness.

The threshold current, peak emission wavelength, and spectral linewidth dependence on grating order shown in Figures 31, 33, and 34, respectively, can also be examined in terms of dependence on the grating fill factor. The 25% fill factor lasers seem to exhibit an unexpected trend of decreasing linewidth with increased grating order in Figure 34a) and 34b). This likely cannot be explained by the oscillatory behavior seen in Chapter 3 for the gratings with fill factors other than 50%, since the experimental trend exists over a larger span of grating orders than would correspond of one period of the sine term in the prediction, which is eight grating orders. The 25% fill factor grating lasers also have a tendency to exhibit two distinct spectral peaks, complicating the curve fitting, and suggesting that multiple lasing lines, rather than linewidth reduction, are encouraged by the 25% fill factor gratings.

In sharp contrast to the 25% fill factor linewidth results, the 75% fill factor lasers exhibit increasing linewidth with increasing grating order in Figure 34a) and 34b). As shown earlier in the theory, with little material removed in the etching process, the 75% fill factor gratings experience a rapid decrease in coupling coefficient as the grating order gets larger. The rapidly increasing linewidth observed in the experimental results is most likely due to this drop in coupling coefficient. These designs also were fabricated at the edge of the wafer, which can possibly explain the larger divergence the linewidth values have from the control averages.

The largest number of buried DFB lasers tested have 50% fill factor gratings. We compare the linewidth reduction measured from these grating lasers at 3 A to the high-order grating model

developed in Chapter 3, to perform a grating parameter sensitivity analysis. This is shown in

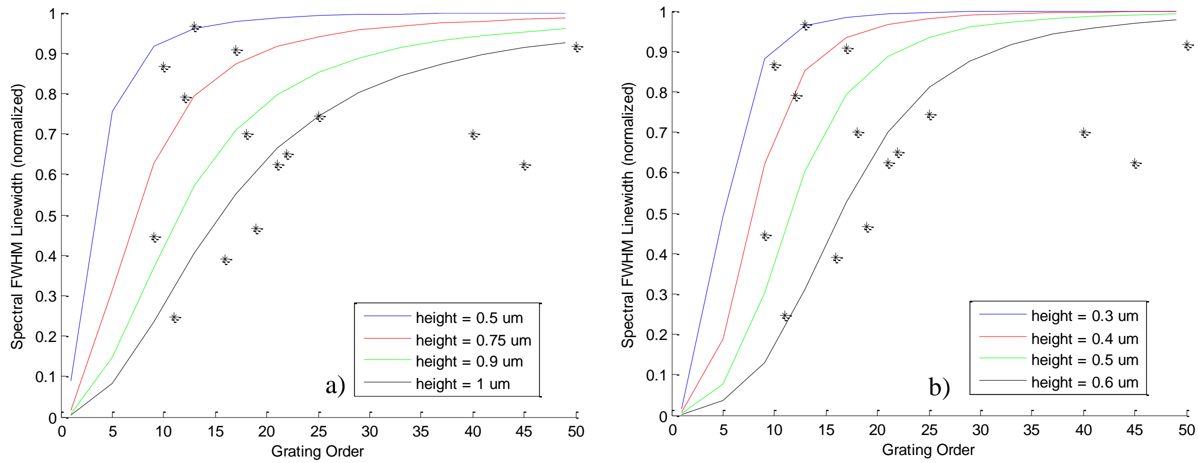

Figure 36: Graphs of the curves from the theoretical prediction of spectral FWHM and the experimentally measured values for fabricated laser devices. The black stars are the experimental points for the 50% fill factor lasers. The curves correspond to the grating tooth heights listed in the legend for each plot. Note that the values differ between the plots for: a) uncoated lasers and b) coated lasers.

Figure 36 for the uncoated and coated laser estimates, where varying grating strength (grating height) is considered (similar to Figure 9 in Chapter 3). Figure 36 is the key result of this dissertation and summarizes the influence of longitudinal mode reduction.

In Figures 34a) and 36a) for the 50% fill factor gratings operating at 3 A, all of the spectral measurements for the grating lasers exhibited linewidths less than the control laser average. Note that all of the buried grating lasers should correspond to the same value of grating height, (since the grating thickness was fixed for all lasers) which is not apparent in the data displayed in Figure 36. The range of tooth height values that span the experimental points can be considered a measure of the interaction strength between grating and the longitudinal mode(s). The coated laser comparison in Figure 36a) shows relatively strong grating interaction is necessary to account for the linewidth reduction for uncoated lasers. However, there is substantial variation of linewidth observed even for small changes in grating order. This variation likely arises from phase requirements that have not been included in the model of Chapter 3. In Figure 36b), the comparison

of measured linewidths to the uncoated laser estimates shows that smaller grating interaction is needed, which is consistent with the analysis in Chapter 3 that the lack of laser coating reduces the impact of the grating.

Buried grating DFB laser diodes emitting near 1550 nm have been successfully fabricated and characterized in terms of threshold current, emission peak wavelength, and spectral linewidth. By normalizing both theory and experimental linewidths to the control lasers which lack a grating, the dependence of the emission linewidth with grating order can be determined. The experimental results, particularly at drive currents above but near threshold, support the conclusion that higher-order gratings do show a reduction of longitudinal modes. Moreover, employing higher-order gratings combined with alternative optical lithography techniques implies a high degree of manufacturability. However, all of the buried grating lasers showed lower output power and reduced slope efficiency as compared to the control lasers, which is consistent with the higher threshold currents shown in Figure 31. Further optimization of the grating design to reduce scattering loss will be necessary for the mode reduction advantages of higher-order buried gratings to enable brightness enhancement.

CHAPTER 6: CONCLUSIONS AND FUTURE WORK

6.1 Summary

To design a diode laser for pumping fiber lasers at 15xx nm, it is desirable to promote broad-area lasers with narrow spectral linewidth and small far-field profile (reduced divergence). To achieve a balance of high power and narrow spectral linewidth, weak DFB gratings can be utilized to reduce the number of lasing longitudinal modes without introducing significant loss. Throughout the literature, both surface-etched and buried DFB gratings have been employed to reduce the number of lasing longitudinal modes in laser diodes. For the vast majority of designs, the objective has been to achieve a single longitudinal mode with high side mode suppression, often for dense wavelength division multiplexing applications. Prior research on high power laser diodes has generally been for shorter infrared wavelengths compatible with GaAs substrates. In this thesis, DFB laser diodes emitting at 15xx nm using high-order gratings have been designed, fabricated, and characterized. This work further prioritizes producing DFB gratings via high volume manufacturable techniques, to enable low-cost broad-area high power lasers.

A theoretical model for determining the spectral linewidth of the laser grating design is presented in Chapter 3 to serve as a qualitative design aid (but not a quantitative predictive tool). An upper bound estimate of the coupling coefficient is found using a buried grating model. From the coupling coefficient the effective reflectivity imparted from the grating is determined for uncoated and coated laser diodes. The impact of the DFB grating is hindered by the native facet reflectivity of semiconductor lasers that lack facet coatings. The difference between coated/uncoated lasers makes it necessary to optimize design for either case separately.

The fabrication process for surface and buried grating edge-emitting lasers is explained in detail in Chapter 4. Fabricating DFB grating lasers is well established in the photonic industry, but this is the first edge-emitting semiconductor laser project for the Photonic Device Research Group. Thus, the fabrication process for the lasers evolved during the research. The surface-etched grating laser process is simpler than the buried gratings, principally because there is no regrowth step. However, the regrown grating lasers were found to be far superior to the surface-etched devices, presumably due to reduced optical loss contributed from the grating. The alternative lithography methods considered are likely candidates for definition of the high-order gratings and are promising directions for continuation of this research project.

The fabricated buried grating lasers were characterized in Chapter 5 using a die-level testing setup and quasi-CW current injection. The edge-emitting characterization setup is also new to the Photonic Device Research Group and was constructed for this project. Data acquisition programs have been developed for ease of data analysis. Only the buried grating DFB lasers were found to be experimentally viable, and were characterized in terms of threshold current, peak emission wavelength, and spectral linewidth (the latter requiring Gaussian curve fitting). The threshold current was shown to be unilaterally larger for the grating lasers than the average of the control lasers. The buried grating lasers, disregarding improperly fabricated devices, all had reasonable thresholds (< 3 A) that were higher, but not excessively so, than control lasers fabricated on the same die but without gratings. The spectral linewidths measured for buried grating lasers were nearly all less than the control lasers at a 3 A drive current, demonstrating the reduction of longitudinal modes. The high-order gratings have been shown to be compatible with manufacturable optical lithography techniques. The most successful DFB designs had a 50% fill factor for which the emission linewidths compare reasonably well to the theoretical estimates.

This work has demonstrated 1.5 μm lasers with spectral narrowing via DFB gratings, fabricated using techniques amenable with large-scale production, for the application of pumping fiber lasers. A compromise between narrow linewidth and high power has led to the implementation of high-order DFB gratings for mode control. While the designs demonstrated in this work have not been optimized with respect to optical loss, high-order gratings appear promising for future high power laser diode applications.

6.2 Future Work

There are other related topics that have been encountered during, but beyond the scope of this project, that are proposed for future study. First, the replacement of e-beam lithography is a principal motivation of this research. Hence, further development of direct UV laser writing and VUV microplasma lithography should be pursued. These methods are significantly less expensive, while yet still being conducive to large-scale, high-volume production.

Secondly, the analysis of Chapter 3 suggests that for periodic gratings, a transition toward higher fill factor and larger tooth height gratings to achieve the same coupling coefficient but with lower loss. Note that higher fill factor implies a larger balance of the high index material in the grating. The modeling framework provided in Chapter 3, can be used to select optimal grating order and fill factor combinations. The local maxima in the coupling coefficient can be utilized to maximize grating strength, while minimizing loss and the feature size requirement.

Thirdly, moving beyond the designs considered here, there are other DFB structures that also could also be pursued to be more manufacturable. For example, a transition to sampled [11] and aperiodic gratings [19] could be made to further lower the loss introduced by DFB gratings,

by replacing less of the high index material. The loss reduction is necessary in order to achieve the brightness enhancement desired for future applications of high power laser diodes.

REFERENCES

[1] H. Joachim, E. Jürgen, and O. Lux, *Lasers Basics, Advances and Applications*, Cham, Switzerland: Springer Nature, 2018.

[2] P. Crump *et al.*, "High-power, high-efficiency monolithic edge-emitting GaAs-based lasers with narrow spectral widths," in *Semiconductors and Semimetals*, 1st ed., vol. 86, Elsevier Inc., 2012, pp. 49–91.

[3] D. J. Richardson, J. Nilsson, and W. A. Clarkson, "High power fiber lasers: Current status and future perspectives," *J. Opt. Soc. Am. B*, vol. 27, no. 11, pp. 63–92, 2010.

[4] J. Fricke et al., "High-power 980-nm broad-area lasers spectrally stabilized by surface Bragg gratings," *IEEE Photonics Technol. Lett*., vol. 22, no. 5, pp. 284–286, 2010.

[5] H. Ghafouri-Shiraz and B. S. K. Lo, *Distributed Feedback Laser Diodes: Principles and Physical Modeling*, Chichester, England: John Wiley & Sons, 1996.

[6] M. Fallahi and R. Bedford, "High-power semiconductor lasers," in *Semiconductor Lasers*, Cambridge, UK: Woodhead Publishing, 2013, pp. 81–120.

[7] W. Streifer, D. R. Scifres, and R. D. Burnham, "Coupling coefficients for distributed feedback single and double-heterostructure diode lasers," *IEEE J. Quantum Electron*., vol. 11, no. 11, pp. 867–873, 1975.

[8] H. Wenzel, J. Fricke, J. Decker, P. Crump, and G. Erbert, "High-power distributed feedback lasers with surface gratings: Theory and experiment," *IEEE J. Sel. Top. Quantum Electron.,* vol. 21, no. 6, pp. 352–358, 2015.

[9] C. Vieu *et al*., "Electron beam lithography: Resolution limits and applications," *Appl. Surf. Sci.,* vol. 164, no. 1–4, pp. 111–117, 2000.

[10] C. M. Schultz *et al*., "11 W broad-area 976 nm DFB lasers with 58% power conversion efficiency," *Electron. Lett.,* vol. 46, no. 8, pp. 580–581, 2010.

[11] Freedom Photonics, Inc. (Santa Barbara, CA), private communication, 2018-2020.

[12] Y. Shi, S. Li, J. Li, L. Jia, S. Liu, and X. Chen, "An apodized DFB semiconductor laser realized by varying duty cycle of sampling Bragg grating and reconstruction-equivalent-chirp technology," *Opt. Commun*., vol. 283, no. 9, pp. 1840–1844, 2010.

[13] *µPG 101 Micro Pattern Generator*, Heidelberg Instruments, Heidelberg, Germany, 2015.

[14] H. Kogelnik and C. V. Shank, "Stimulated emission in a periodic structure," *Appl. Phys. Lett*., vol. 18, no. 4, pp. 152–154, 1971.

[15] M. Nakamura, K. Aiki, J. Umeda, A. Yariv, and T. Morikawa, "GaAs-GaAlAs double-hertostructure distributed-feedback diode lasers," *Appl. Phys. Lett*., vol. 25, no. 487, pp. 487–488, 1974.

[16] D. R. Scifres, R. D. Burnham, and W. Streifer, "Distributed-feedback single heterojunction GaAs diode laser," *Appl. Phys. Lett*., vol. 25, no. 4, pp. 203–206, 1974.

[17] M. Nakamura, K. Aiki, J. Umeda, and A. Yariv, "CW operation of distributed-feedback GaAs-GaAlAs diode lasers at temperatures up to 300 K," *Appl. Phys. Lett*., vol. 27, no. 7, pp. 403–405, 1975.

[18] C. M. Schultz *et al*., "In situ etched gratings embedded in AlGaAs for efficient high power 970 nm distributed feedback broad-area lasers," *Appl. Phys. Lett*., vol. 100, no. 20, 2012.

[19] J. Decker, J. Fricke, A. Maaßdorf, G. Erbert, G. Tränkle, and P. Crump, "Non-uniform DFB-surface-etched gratings for enhanced performance high power, high brightness broad-area lasers," in *Proc. of SPIE*, vol. 10086, pp. 1–8, February, 2017.

[20] K. Dridi, A. Benhsaien, J. Zhang, and T. J. Hall, "Narrow linewidth 1550 nm corrugated ridge waveguide DFB lasers," *IEEE Photonics J.*, vol. 26, no. 12, pp. 1192–1195, 2014.

[21] K. D. Choquette, M. Hong, R. S. Freund, S. N. G. Chu, J. Mannaerts, and R. Wetzel, "Molecular beam epitaxial regrowth on *in situ* etched AlAs/AlGaAs heterostructures," *Appl. Phys. Lett.*, vol. 60, pp. 1738-1740, 1992.

[22] K. D. Choquette, R. J. Shul, A. J. Howard, and D. J Rieger, R. Freund and R. Wetzel, "Smooth reactive ion etching of GaAs using a hydrogen plasma pretreatment," *J. Vac. Sci. Technol.*, vol. B13, no. 40, 1995.

[23] R. A. Gottscho and C. W. Jurgensen, "Microscopic uniformity in plasma etching," *J. Vaccuum Sci. Technol. B*, vol. 10, no. 5, pp. 2133–2143, 1992.

[24] J. Fricke et al., "DFB lasers with apodized surface gratings for wavelength stabilization and high efficiency," *Semicond. Sci. Technol.,* vol. 32, no. 7, 2017.

[25] J. Fricke *et al.*, "High-power distributed feedback lasers with surface gratings," *IEEE Photonics Technol. Lett.*, vol. 24, no. 16, pp. 1443–1445, 2012.

[26] T. J. Slight *et al.*, "InGaN/GaN laser diodes with high-order notched gratings," *IEEE Photonics Technol. Lett.*, vol. 29, no. 23, pp. 2020–2022, 2017.

[27] J. H. Kang *et al.*, "DFB laser diodes based on GaN using 10th order laterally coupled surface gratings," *IEEE Photonics Technol. Lett.*, vol. 30, no. 3, pp. 231–234, 2018.

[28] L. Liu, H. W. Qu, Y. Wang, Y. Liu, Y. J. Zhang, and W. H. Zheng, "High-brightness single-mode double-tapered laser diodes with laterally coupled high-order surface grating," *Opt. Lett.*, vol. 39, no. 11, pp. 3231–3234, 2014.

[29] M. Kamp *et al.*, "Lateral coupling: A material independent way to complex coupled DFB lasers," *Opt. Mater.*, vol. 17, no. 1–2, pp. 19–25, 2001.

[30] A. Abdullaev, Q. Lu, W. Guo, M. J. Wallace, M. Nawrocka, F. Bello, A. Benson, J. O'Callaghan, and J. F. Donegan, "Improved performance of tunable single-mode laser array based on high-order slotted surface grating," *Opt. Express*, vol. 23, no. 9, pp. 12072–8, 2015.

[31] T. Yu, L. Zou, L. Wang, and J. J. He, "Single-mode and wavelength tunable lasers based on deep-submicron slots fabricated by standard UV-lithography," *Opt. Express*, vol. 20, no. 15, pp. 16291–16299, 2012.

[32] K. Shi, F. Smyth, D. Reid, B. Roycroft, B. Corbett, F. H. Peters, and L. P. Barry, "Characterization of a tunable three-section slotted Fabry-Perot laser for advanced modulation format optical transmission," *Opt. Commun.*, vol. 284, no. 6, pp. 1616–1621, 2011.

[33] J. Decker, P. Crump, J. Fricke, A. Maassdorf, G. Erbert, and G. Trankle, "Narrow stripe broad-area lasers with high-order distributed feedback surface gratings," *IEEE Photonics Technol. Lett.,* vol. 26, no. 8, pp. 829–832, 2014.

[34] M. Kamp, J. Hofmann, A. Forchel, F. Schafer, and J. P. Reithmaier, "Low-threshold high-quantum-efficiency laterally gain-coupled InGaAs / AlGaAs distributed feedback lasers," *Appl. Phys. Lett.*, vol. 74, no. 483, pp. 483–485, 1999.

[35] J. Viheriälä *et al.*, "Applications of UV-nanoimprint soft stamps in fabrication of single-frequency diode lasers," *Microelectron. Eng.*, vol. 86, no. 3, pp. 321–324, 2009.

[36] J. Fricke *et al.*, "Properties and fabrication of high-order Bragg gratings for wavelength stabilization of diode lasers," *Semicond. Sci. Technol.,* vol. 27, no. 5, pp. 6–11, 2012.
[37] L. R. Harriott, "Limits of lithography," *Proc. IEEE*, vol. 89, no. 3, pp. 366–374, 2001.
[38] O. Svelto, S. Longhi, G. Della Valle, and G. Huber, "Lasers and coherent light sources," in *Handbook of Lasers and Optics*, 2nd ed., Berlin, Germany: Springer-Verlag, 2012, p. 775.
[39] W. Zheng and G. W. Taylor, "Determination of the photon lifetime for DFB lasers," *IEEE J. Quantum Electron*., vol. 43, no. 4, pp. 295–302, 2007.
[40] W. Streifer, D. R. Scifres, and R. D. Burnham, "Longitudinal mode spectra of diode lasers," *Appl. Phys. Lett.,* vol. 40, no. 4, pp. 305–307, 1982.
[41] R. Kumar, private communication, Sept.-Dec. 2020.
[42] S. J. Park, C. M. Herring, A. E. Mironov, J. H. Cho, and J. G. Eden, "25 W of average power at 172 nm in the vacuum ultraviolet from flat, efficient lamps driven by interlaced arrays of microcavity plasmas," *APL Photonics*, vol. 2, no. 4, 2017.

APPENDIX: EDGE-EMITTING LASER FABRICATION PROCESS

Process Sheet: Surface Grating InP Edge-Emitting Lasers

Step	Process	Details
0. ______	Cleave	Cleave, degrease
1. ______	SiO_2 Deposition:	Trion PECVD: Low dep (360 s) for 200 nm
2. ______	Longitudinal Grating Photolithography:	Degrease Dehydration bake 270°C for 2 min HMDS vapor prime (CRITICAL) AZ 1505 spin 10000 rpm, 5000 rpm/s, 30 s Bake 110°C for 1 min Edge bead removal – Use swab with acetone to remove Mask: 3" Quartz EEL Longitudinal Grating Mask Expose: 15 s (aligner A at 9 mW/cm^2) Power: ______W; Time: ______s Develop in undiluted AZ 917 MIF (~8 s): _____s
3. ______	SiO_2 Etch:	O_2 plasma descum (250 W for 30 s) Oxford Freon Recipe: *Choquette SiO_2 Selective* (3 mT, 25/700 W, CHF_3 50 sccm, 2 min (125 nm/min)) Time: ______ min Check for conductivity to confirm sufficient etch-back Remove PR mask using 1000 W 5 min descum Alpha-step: _______
4. ______	Grating Etch:	1:10 NH_4OH:DI dip for 20 s and decant Oxford Chlorine Base Recipe: *Choquette InP Etch Raman* (4 mT, 100/1000 W, Cl_2:CH_4:H_2 10:8:4 sccm, 1 min 25 s)
5. ______	SiO_2 Mask Removal:	Use BOE (10:1 or 6:1 from 444 lab) for 2 min Time: ______ min Check for conductivity to confirm sufficient etch-back Alpha-step: _______
6. ______	SiO_2 Deposition:	Trion PECVD: Low dep (900 s) for 500 nm
7. ______	Waveguide Photolithography:	Degrease Dehydration bake 270°C for 2 min HMDS vapor prime AZ 5214 spin 3 s 500 rpm, 30 s 4000 rpm Bake 110°C for 45 s

Edge bead removal – 1 min on Aligner C, Develop ~1 min 1:4 AZ 400K:DI
Mask: 4" Quartz EEL Long Grating Waveguide
Expose: 40 s (aligner A at 9 mW/cm^2)
Power: ______W; Time: ______s
Reversal bake 110ºC for 45 s
Flood exposure on Aligner C for 15 s (use HP mode)
Develop in undiluted AZ 917 MIF (~40 s): _____s

8. ______SiO_2 Etch:

O$_2$ plasma descum (250 W for 3 min)
Oxford Freon Recipe: *Choquette SiO_2 Selective* (3 mT, 25/700 W, CHF_3 50 sccm, 5 min (125 nm/s))
Time: ______ min
Check for conductivity to confirm sufficient etch-back
Remove PR mask using 1000 W 5 min descum
Alpha-step: _______

9. ______ Contact Photolithography:

Degrease
O_2 plasma descum (1000 W for 2 min)
Dehydration bake 110ºC for 5 min
LOR 30B spin 4 s 400 rpm, 60 s 3000 rpm
Manual edgebead removal with razor blade
Bake 170ºC 5 min
AZ 5214 spin 3 s 500 rpm, 30 s 4000 rpm
Bake 110ºC for 45 s
Edge bead removal – 1 min on Aligner C, Develop ~1 min 1:4 AZ 400K:DI
Mask: 4" Quartz EEL Long Grating Contact
Expose: 40 s (aligner A at 9 mW/cm^2)
Power: ______W; Time: ______s
Reversal bake 110ºC for 45 s
Flood exposure on Aligner C for 15 s (use HP mode)
Develop in undiluted AZ 917 MIF (~40 s): _____s until LOR undercut appears

10. ______p-Metal Deposition:

O_2 plasma descum (250 W for 3 min)
1:10 NH_4OH (ammonia):DI dip for 20 s and decant
Deposit: 150 Å Ti / 1600 Å Au
Actual: ______Å Ti / ______Å Au

11. ______Metal Lift-off and Cleaning:

PG Remover soak
Degrease
O_2 plasma descum (1000 W for 3 min)

12. ______ Send to Freedom Photonics for thinning, backside contact, and cleaving

Process Sheet: Buried Grating InP Edge-Emitting Lasers

0. ______	Cleave	Cleave, degrease
1. ______	SiO_2 Deposition:	Trion PECVD: Low dep (360 s) for 200 nm
2. ______	Fiducial Marker Photolithography:	Degrease Dehydration bake 270ºC for 2 min HMDS vapor prime AZ 1505 spin 10000 rpm, 5000 rpm/s, 30s Bake 110ºC for 1 min Edge bead removal – Use swab with acetone to remove Mask: 4" Quartz Fiducial Mask Expose: 15 s (aligner A at 9 mW/cm^2) Power: ______W; Time: ______s Develop in undiluted AZ 917 MIF (~8 s): _____s
3. ______	SiO_2 Etch:	O_2 plasma descum (250 W for 30 s) Oxford Freon Recipe: *Choquette SiO_2 Selective* (3 mT, 25/700W, CHF_3 50 sccm, 2 min (125 nm/min)) Time: ______ min Check for conductivity to confirm sufficient etch-back Remove PR mask using 1000 W 5 min descum Alpha-step: _______
4. ______	Fiducial Mark Etch:	1:10 NH_4OH:DI dip for 20 s and decant Oxford Chlorine Base Recipe: *Choquette InP Etch Raman* (4 mT, 100/1000 W, Cl_2:CH_4:H_2 10:8:4 sccm)
5. ______	SiO_2 Mask Removal:	Use BOE (10:1 or 6:1 from 444 lab) for 2 min Time: ______ min Check for conductivity to confirm sufficient etch-back Alpha-step: _______
6. ______	SiO_2 Deposition:	Trion PECVD: Low dep (900 s) for 500 nm
7. ______	Longitudinal Grating Photolithography:	Degrease Dehydration bake 270ºC for 2 min HMDS vapor prime (CRITICAL) AZ 1505 spin 10000 rpm, 5000 rpm/s, 30 s Bake 110ºC for 1 min Edge bead removal – Use swab with acetone to remove Mask: 3" Quartz EEL Longitudinal Grating Mask Expose: 15 s (aligner A at 9 mW/cm^2) Power: ______W; Time: ______s Develop in undiluted AZ 917 MIF (~8 s): _____s

Step	Procedure
8. ______SiO_2 Etch:	O_2 plasma descum (250 W for 30 s) Oxford Freon Recipe: *Choquette SiO_2 Selective* (3 mT, 25/700W, CHF_3 50 sccm, 2 min (125 nm/min)) Time: ______ min Check for conductivity to confirm sufficient etch-back Remove PR mask using 1000 W 5 min descum Alpha-step: _______
9. ______Grating Etch:	1:10 NH_4OH:DI dip for 20 s and decant Oxford Chlorine Base Recipe: *Choquette InP Etch Raman* (4 mT, 100/1000 W, Cl_2:CH_4:H_2 10:8:4 sccm)
10. ______SiO_2 Mask Removal:	Use BOE (10:1 or 6:1 from 444 lab) for 2 min Time: ______ min Check for conductivity to confirm sufficient etch-back Alpha-step: _______
11. ______Clean:	Complete this step immediately before regrowth! Manually swab clean and degrease O_2 plasma descum (1000 W for 5 min) BOE etch 10:1 for 2 min
12. ______Regrowth:	Hand-off for MOCVD regrowth
13. ______SiO_2 Deposition:	Trion PECVD: Low dep (900 s) for 500 nm
14. ______Waveguide Photolithography:	Degrease Dehydration bake 270°C for 2 min AZ 5214 spin 3 s 500 rpm, 30 s 4000 rpm Bake 110°C for 45 s Edge bead removal – 1 min on Aligner C, Develop ~1 min 1:4 AZ 400K:DI Mask: 4” EEL Long Grating Waveguide Expose: 40 s (aligner A at 9 mW/cm^2) Power: ______W; Time: ______s Reversal bake 110°C for 45 s Flood exposure on Aligner C for 15 s (use HP mode) Develop in undiluted AZ 917 MIF (~40 s): _____s
15. ______SiO_2 Etch:	O_2 plasma descum (250 W for 3 min) Oxford Freon Recipe: *Choquette SiO_2 Selective* (3 mT, 25/700W, CHF_3 50 sccm, 5 min (125 nm/s)) Time: ______ min Check for conductivity to confirm sufficient etch-back Remove PR mask using 1000 W 5 min descum

Alpha-step: _______

16. ______ Contact Photolithography:

Degrease
O_2 plasma descum (1000 W for 2 min)
Dehydration bake 110ºC for 5 min
LOR 30B spin 4 s 400 rpm, 60 s 3000 rpm (gives 3 µm thickness, sufficient for 2 µm of gold)
Manual edge bead removal with razor blade
Bake 170ºC 5 min
AZ 5214 spin 3 s 500 rpm, 30 s 4000 rpm
Bake 110ºC for 45 s
Edge bead removal – 1 min on Aligner C, Develop ~1 min 1:4 AZ 400K:DI
Mask: 4” Quartz EEL Long Grating Contact
Expose: 40 s (aligner A at 9 mW/cm^2)
Power: ______W; Time: ______s
Reversal bake 110ºC for 45 s
Flood exposure on Aligner C for 15 s (use HP mode)
Develop in undiluted AZ 917 MIF (~40 s): _____s until LOR undercut appears

17. ______p-Metal Deposition:

O_2 plasma descum (250 W for 3 min)
1:10 NH_4OH (ammonia):DI dip for 20 s and decant
Deposit: 150 Å Ti / 1600 Å Au
Actual: ______Å Ti / ______Å Au

18. ______Metal Lift-off and Cleaning:

PG Remover soak
Degrease
O_2 plasma descum (1000 W for 3 min)

19. ______ Send to Freedom Photonics for thinning, backside contact, and cleaving